ChemComm

ROYAL SOCIETY OF CHEMISTRY

FEATURE ARTICLE

View Article Online
View Journal | View Issue

Cite this: *Chem. Commun.*, 2021, **57**, 7743

Perfluoro-*tert*-butanol: a cornerstone for high performance fluorine-19 magnetic resonance imaging

Tingjuan Wu,†[a] Anfeng Li,†[a] Kexin Chen,[a] Xingxing Peng,[a] Jing Zhang,[b] Mou Jiang,[c] Shizhen Chen,[c] Xing Zheng,*[a] Xin Zhou *[c] and Zhong-Xing Jiang *[ab]

Received 13th May 2021,
Accepted 24th June 2021

DOI: 10.1039/d1cc02133h

rsc.li/chemcomm

As a versatile quantification and tracking technology, ^{19}F magnetic resonance imaging (^{19}F MRI) provides quantitative "hot-spot" images without ionizing radiation, tissue depth limit, and background interference. However, the lack of suitable imaging agents severely hampers its clinical application. First, because the ^{19}F signals are solely originated from imaging agents, the relatively low sensitivity of MRI technology requires high local ^{19}F concentrations to generate images, which are often beyond the reach of many ^{19}F MRI agents. Second, the peculiar physicochemical properties of many fluorinated compounds usually lead to low ^{19}F signal intensity, tedious formulation, severe organ retention, *etc.* Therefore, the development of ^{19}F MRI agents with high sensitivity and with suitable physicochemical and biological properties is of great importance. To this end, perfluoro-*tert*-butanol (**PFTB**), containing nine equivalent ^{19}F and a modifiable hydroxyl group, has outperformed most perfluorocarbons as a valuable building block for high performance ^{19}F MRI agents. Herein, we summarize the development and application of PFTB-based ^{19}F MRI agents and analyze the strategies to improve their sensitivity and physicochemical and biological properties. In the context of PFC-based ^{19}F MRI agents, we also discuss the challenges and prospects of PFTB-based ^{19}F MRI agents.

1. Introduction

Magnetic resonance imaging is one of the most used medical imaging technologies for disease diagnosis and therapy assessment,[1] because it provides high-resolution images non-invasively without ionizing radiation and tissue depth limit.[2] As water accounts for over 60% of body weight, imaging its local concentration and relaxation states provides valuable anatomical and physiological information. Consequently, ^{1}H MRI using water protons as the signal source is overwhelmingly used in the clinic. However, the ubiquitous water in biological systems also generates high background signals, leading to difficulty in distinguishing the region of interest from its surrounding region, *e.g.*, diseased and normal tissues. Thus, many ^{1}H MRI contrast agents (CAs) have been developed to enhance the visibility of the region of interest by affecting the relaxation of water.[3] Longitudinal CAs decrease the longitudinal relaxation times (T_1) and brighten the region, while transverse CAs reduce the transverse relaxation times (T_2) and darken the area. Although widely used in the clinic, CAs still suffer from many drawbacks, such as double imaging process, high dose, and toxicity.[4] Furthermore, it is unreliable for CA-assisted ^{1}H MRI to quantify the targets of interest in biological systems, such as drugs, biomolecules, nanoparticles, *etc.*, because CA-modulated water ^{1}H signals are indirectly related to the concentration of targets.[5] On the other hand, direct quantification with ^{1}H signals of targets in biological systems is hampered by weak ^{1}H signals of targets, strong background signals, and overcrowded ^{1}H signals within a chemical shift range of about 20 ppm, which severely mask the ^{1}H signals of targets.

^{19}F MRI has emerged as a valuable complement to ^{1}H MRI, which overcomes many drawbacks of ^{1}H MRI and gains extensive application as a quantification and tracking technology.[5–7] (1) ^{19}F is a nucleus of choice for MRI, which is the second most sensitive stable nucleus for MRI with 100% natural abundance

[a] *Group of Lead Compound, Department of Pharmacy, Hunan Provincial Key Laboratory of Tumor Microenvironment Responsive Drug Research, Hunan Province Cooperative Innovation Center for Molecular Target New Drug Study, University of South China, Hengyang 421001, Hunan, China. E-mail: zhengxing9166@sohu.com*

[b] *Hubei Province Engineering and Technology Research Center for Fluorinated Pharmaceuticals, School of Pharmaceutical Sciences, Wuhan University, Wuhan 430071, China. E-mail: zxjiang@whu.edu.cn*

[c] *State Key Laboratory of Magnetic Resonance and Atomic and Molecular Physics, National Center for Magnetic Resonance in Wuhan, Wuhan Institute of Physics and Mathematics, Innovative Academy of Precision Measurement Science and Technology, Chinese Academy of Sciences, Wuhan, Wuhan 430071, China. E-mail: xinzhou@wipm.ac.cn*

† The authors contributed equally to this work.

and 83% sensitivity of ^{1}H. (2) Fluorinated organic compounds (FOCs) have a wide chemical shift range of about 250 ppm and the chemical shift is sensitive to the local environment, molecular structure, and target interactions, which lays the foundation for many valuable ^{19}F MRI probes.[8,9] (3) FOCs comprise a huge family, including 20% of marketed drugs,[10] 16% of marketed agrochemicals,[11] and numerous fluorinated chemicals,[12] which provide a variety of agents for ^{19}F MRI. (4) FOCs are absent from most biological systems. In humans, only a trace of fluorinated inorganic compounds exists in bone and teeth, which regular ^{19}F MRI instruments can hardly detect due to very short T_2. Thus, there is no endogenous ^{19}F signal in biological systems, making ^{19}F MRI an ideal "hot spot" imaging technology to track targets. (5) ^{19}F signals are solely originated from fluorinated agents and their intensities are directly proportional to local ^{19}F concentrations, facilitating the accurate ^{19}F MRI quantification of fluorinated targets.[5]

Although only four years younger than ^{1}H MRI,[13] ^{19}F MRI has not been used in the clinic mainly due to the lack of suitable ^{19}F MRI agents. A low millimolar concentration of effective local ^{19}F ($^{19}F_{eff}$) is usually required for ^{19}F MRI to generate images. Notably, $^{19}F_{eff}$ refers to the portion of ^{19}F generating ^{19}F images, not all ^{19}F in a FOC ($^{19}F_{total}$). Due to the non-equivalent arrangement of ^{19}F, most FOCs give multiple ^{19}F signals with a wide chemical shift distribution.[14] During ^{19}F MRI, the most prominent ^{19}F peak is usually selected for ^{19}F MRI to improve the signal intensity and sensitivity. In contrast, the rest of the ^{19}F peaks don't contribute to ^{19}F MRI but generate chemical shift imaging artifacts. So, instead of increasing $^{19}F_{total}$ or fluorine content (^{19}F%) in ^{19}F MRI agents, it is better to improve signal intensity by avoiding ^{19}F signal splitting and increasing $^{19}F_{eff}$. Therefore, ideal ^{19}F MRI agents should have as many $^{19}F_{eff}$ as possible and a single ^{19}F peak.

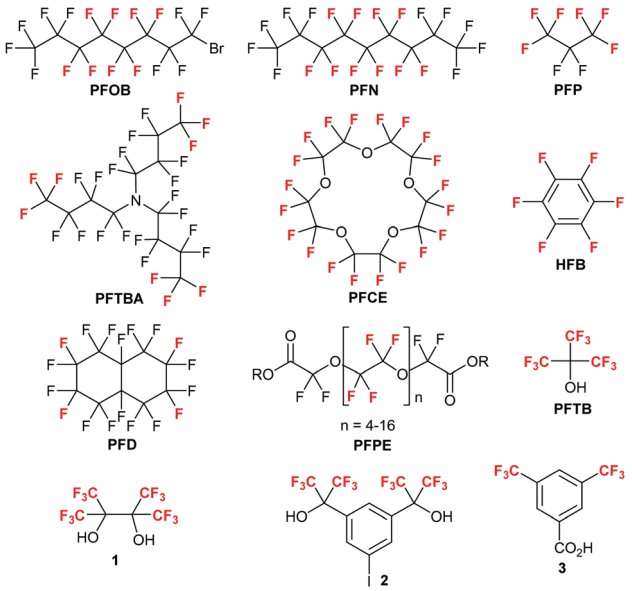

Fig. 1 Structures of fluorinated chemicals used in ^{19}F MRI.

It is noteworthy that these PFCs were not designed for ^{19}F MRI, which suffer from many drawbacks in ^{19}F MRI. (1) Because PFCs are very hydrophobic and immiscible in water, PFCs are usually formulated into water-soluble nanoparticles (NPs) as ^{19}F MRI agents, which involves complex formulation and characterization processes.[16] (2) PFCs usually have severe organ retention, and they tend to accumulate in the liver, spleen, and lungs and stay in these organs for many months.[17,18] The long *in vivo* resident times lead to strong background signals and misleading information for further ^{19}F MRI study on the same object. Although PFCs are biologically inert, severe organ retention may also lead to biological problems like tissue hypoxia.[19,20] (3) It is difficult to modify these PFCs for multifunction or better physicochemical properties due to the lack of modifiable groups and very abnormal reactivity.

2. ^{19}F MRI agents

2.1. Perfluorocarbons directly used in ^{19}F MRI

Since 1977, many perfluorocarbons (PFCs) have been used in ^{19}F MRI (Fig. 1), including perfluorooctyl bromide (**PFOB**), perfluorononane (**PFN**), perfluorotributylamine (**PFTBA**), perfluoropropane (**PFP**), and perfluorodecalin (**PFD**). Although these PFCs have a high $^{19}F_{total}$, they give multiple ^{19}F signals with quite different chemical shifts. During ^{19}F MRI data collection, the acquisition bandwidths are usually set to cover only the strongest signal(s) from the $^{19}F_{eff}$, marked in red in Fig. 1, to achieve the high signal-to-noise ratio (SNR). So, these PFCs have a low $^{19}F_{eff}$. For example, only 4 $^{19}F_{eff}$ out of 18 $^{19}F_{total}$ in **PFD** may contribute to ^{19}F MRI because the ^{19}F signals are split and distributed in a wide chemical shift range. Then, PFCs with all equivalent ^{19}F were employed in ^{19}F MRI, including perfluoro-15-crown-5 (**PFCE**) and hexafluorobenzene (**HFB**). Later, perfluoropolyethers (**PFPE**) with many pseudo-equivalent ^{19}F were used in ^{19}F MRI by Ahrens *et al.*[15]

2.2. Fluorinated building blocks for ^{19}F MRI

The design and synthesis of novel ^{19}F MRI agents with high sensitivity and suitable physicochemical and biological properties overcame many drawbacks of PFC agents. Because direct fluorination involves low yield and harsh reaction conditions, indirect synthesis of ^{19}F MRI agents from fluorinated building blocks is a better strategy. In 2007, perfluoro-*tert*-butanol (**PFTB**, Fig. 1) was first identified by Yu and Jiang as an ideal building block for ^{19}F MRI agents.[21] With a high ^{19}F% of 72.4%, **PFTB** gives a singlet ^{19}F NMR peak from 9 equivalent ^{19}F. Furthermore, under the influence of 3 electron-withdrawing CF_3-groups, the OH-group in **PFTB** is very acidic (pK_a = 5.33),[22] which makes **PFTB** a good nucleophile for S_N2 substitution during ^{19}F MRI agents' synthesis.[21] Later, perfluoropinacol **1** with 12 equivalent ^{19}F and 2 acidic OH groups (pK_{a1}: 5.95, pK_{a2}: 10.43)[22] was employed as a building block for water-soluble and sensitive ^{19}F MRI agents, but the agents suffered from acute toxicity.[23] Recently, iodobenzene **2** with 12 equivalent ^{19}F and benzoic acid **3** with 6 equivalent ^{19}F were employed as the key

building blocks for ^{19}F MRI-traceable peptides[24,25] and dendrimers.[26–28] Among these, **PFTB** is the most promising one due to its easy availability and modification, and high F% and $^{19}F_{eff}$.

3. Synthesis of PFTB–^{19}F MRI agents

3.1. Property and preparation of PFTB

PFTB is a volatile liquid with a low boiling point of 45 °C and a high density of 1.693 g mL^{-1}. It has acute toxicity and causes skin and eye irritation, probably due to its acidity and volatility. However, **PFTB** reacts with NaOH solutions to give water-soluble NaOC(CF$_3$)$_3$ in quantitative yield, which is a non-volatile and stable white powder, much easier to store and handle than **PFTB**.

Although **PFTB** is commercially available, there are many methods for laboratory preparation (Scheme 1). In 1965, **PFTB** was first synthesized by oxidation of perfluoro-2-nitroso-2-methylpropane **4** by Dyatkin *et al.*[29] Then, Filler *et al.* developed a nucleophilic addition–fluorination method, but it suffered from harsh reaction conditions and low yield.[30] Later, Pavlik *et al.* prepared **PFTB** by treating perfluoroisobutene oxide **6** with HF in the presence of SbF$_5$.[31] In 1992, Kotun *et al.* developed a convenient nucleophilic addition method for **PFTB**.[32] Kotun's method avoided harsh reaction conditions and dangerous chemicals, and was adopted in this lab for 100 gram scale preparation of **PFTB**.

3.2. Strategies to introduce PFTB into ^{19}F MRI agents

Due to its high chemical and biological stability, the ether bond is very fit for introducing **PFTB** into ^{19}F MRI agents (Scheme 2). **PFTB** and NaOC(CF$_3$)$_3$ are excellent nucleophiles and thus suitable substrates for Williamson ether synthesis of aliphatic perfluoro-*tert*-butoxylated (PFTB-) agents.[33–39] (1) With good solubility in THF, NaOC(CF$_3$)$_3$ is a convenient reagent for nucleophilic ring-opening of macrocyclic sulfate **7** in THF to give PFTB-tetraethylene glycol **8** in high yield.[38] (2) For primary alcohols, the Mitsunobu reaction with **PFTB** is an effective method to prepare the corresponding PFTB-ethers under mild conditions.[21,39,40] Performing the reaction in a sealed vessel and in the presence of 4 Å molecular sieves promotes the formation of PFTB-ethers.[21] (3) For aromatic substrates, thermal decomposition of aryldiazonium salts in **PFTB** is the most used strategy to incorporate the PFTB-group.[41,42] However, it involves the explosive aryldiazonium salt intermediates and expensive **PFTB** as the reaction solvent. (4) To address these issues, a diaryliodonium salt-based strategy was recently developed by Zhao *et al.*[43] It is noteworthy that, in contrast to *tert*-butyl ethers, PFTB-ethers are stable to Brønsted acids and Lewis acids, such as HCl, TFA, and AlCl$_3$,[21,44] because of the strong electron-withdrawing nature of the **PFTB**-group.

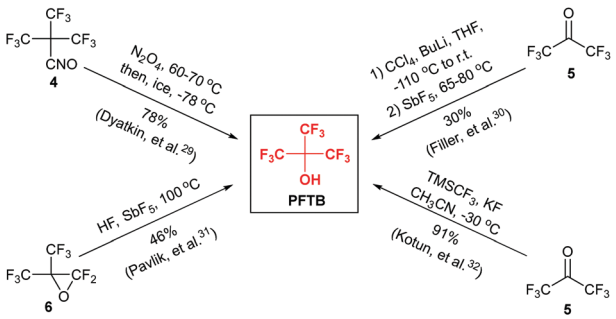

Scheme 1 Methods for **PFTB** preparation.

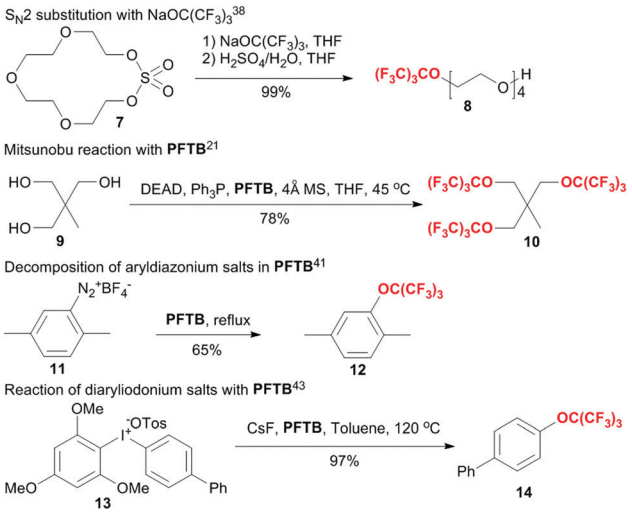

Scheme 2 Strategies to introduce the PFTB-group.

4. Application of PFTB–^{19}F MRI agents

4.1. PFTB-containing bioactive agents

Fluorination of bioactive agents is a well-known drug discovery strategy,[45] which has delivered over 20% of marketed drugs.[10] Fluorination can modulate the physicochemical and biological properties of bioactive agents,[45,46] and facilitate their ^{19}F MRI/NMR investigation.[8,9] Comparing fluorinated drugs on the market,[10] PFTB-bioactive agents are advantageous for ^{19}F MRI due to their high $^{19}F_{eff}$. Many PFTB-bioactive agents have been discovered and their ^{19}F MRI/NMR studies have greatly promoted pharmaceutical, biological and pathological studies (Fig. 2).[41,47–54]

Monitoring the biotransformation of PFTB-substrates to dopamine by aromatic acid decarboxylase (AADC) with ^{19}F MRI/NMR may promote the treatment and diagnosis of Parkinson's disease and brain tumors. PFTB-agents **15–17** have been identified as suitable AADC substrates, but no detailed ^{19}F MRI/NMR of the biotransformation was disclosed (Fig. 2).[48–50] Notably, PFTB-probe **18** was developed for early diagnosis of Alzheimer's disease with ^{19}F MRI, while no ^{19}F NMR signal was detected from probe **18**-treated brain tissue.[41] In these cases, the strong hydrophobic interaction between PFTB-agents and brain tissue severely shortened the T_2 and significantly reduced the ^{19}F signal intensity.

As hypoxia is a pathophysiological characteristic of solid tumors, the substrates of reductases may be tumor-targeted therapeutics or imaging probes.[55] PFTB-indolequinone (IQ-F) probe **19** was developed as a substrate for reductases expressed in tumor cells (Fig. 2).[51] In tumor cells, the reductases catalyzed

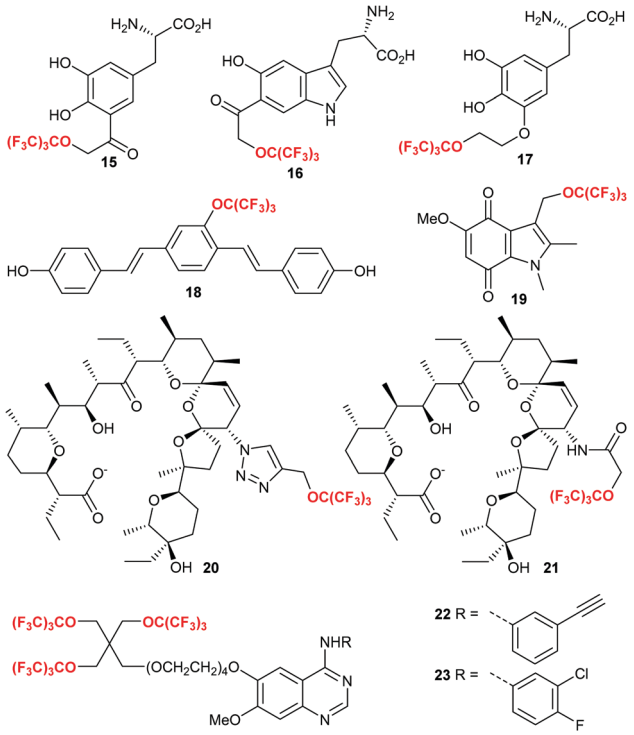

Fig. 2 Structures of bioactive PFTB–^{19}F MRI probes.

the one-electron reduction of probe **19** into IQ accompanied by the release of **PFTB**. Because probe **19** and **PFTB** had distinctive ^{19}F NMR signals ($\Delta\delta \approx 4$ ppm), the biotransformation process was quantitatively monitored by ^{19}F NMR and chemical shift-selected ^{19}F MRI, which quantified the consumption of probe **19** and the release of **PFTB** under hypoxic conditions (Scheme 3). Notably, unless the ether bond is cleaved, the ^{19}F NMR chemical shift changes of PFTB-ethers are not sensitive (<1 ppm) to chemical modifications, biotransformation, or the local environment.

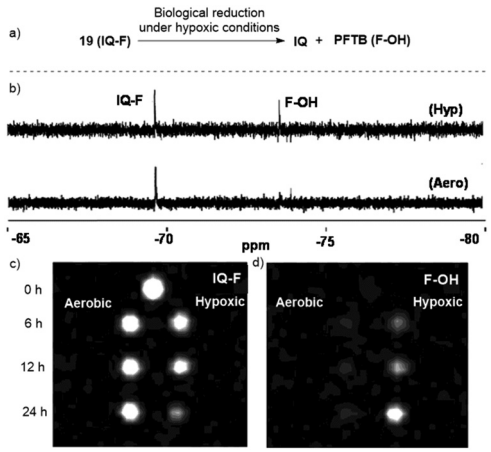

Scheme 3 Monitoring the reduction of **19** in A549 cells under hypoxia and aerobic conditions (a) with ^{19}F NMR (b), **19** signal-selected ^{19}F MRI (c) and **PFTB** signal-selected ^{19}F MRI (d).[51] Reproduced from ref. 51 with permission of American Chemical Society 2009.

Cancer stem cells (CSCs) play essential roles in cancer metastasis and recurrence. The development of selective CSC inhibitors as probes to monitor CSCs with ^{19}F MRI/NMR is of great importance to cancer metastasis intervention and therapy. Salinomycin is a cheap natural product with high selective inhibition towards CSCs.[56] PFTB–salinomycin derivatives **20** and **21** were developed by Jiang *et al.* as promising cancer drug candidates, which showed 2- and 4-times higher potency towards human breast cancer MCF-7 cells than salinomycin, respectively (Fig. 2).[52,53] With a strong singlet ^{19}F NMR peak, PFTB–salinomycin **20** and **21** generated ^{19}F MRI at a low concentration of 5.6 mM (Fig. 3). In this case, the selective introduction of a PFTB-group into salinomycin enhanced the anti-cancer potency and provided ^{19}F MRI/NMR capability for potential CSC research, molecular mechanism study, and cancer therapy. The strategy was recently adopted by Ma *et al.* to develop PFTB$_3$-4-anilinoquinazoline **22** and **23** as potential ^{19}F MRI-traceable EGFR tyrosine kinase inhibitors (Fig. 2), which were detected by ^{19}F MRI at 10 mM.[54]

The development of PFTB-bioactive agents for *in vivo* ^{19}F MRI studies is very challenging because it requires a good balance between bioactivity and ^{19}F MRI sensitivity. (1) The bioactivity of an agent is mainly determined by the delicate interactions between the agent and its target, which is closely related to its chemical structure and physicochemical properties. As a very bulky and highly hydrophobic group, the PFTB-group would considerably impact the bioactivity and pharmacokinetics. (2) PFTB-bioactive agents should generate ^{19}F MRI within its safety window. The *in vivo* concentration of bioactive agents is usually in the micromolar or lower range. On the other hand, the $^{19}F_{eff}$ concentration for ^{19}F MRI is generally in the low millimolar range, which is far beyond the safety window of most bioactive agents. This is probably the main reason there are so many fluorinated drugs on the market while there are so few *in vivo* ^{19}F MRI/NMR studies on them.

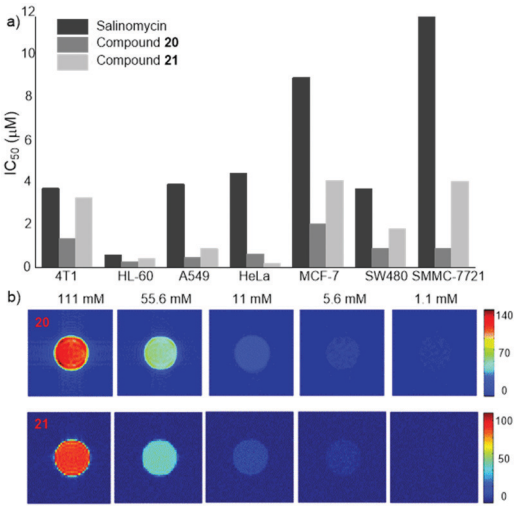

Fig. 3 Cytotoxicity (a) and ^{19}F MRI phantom images (b) of PFTB–salinomycin derivatives **20** and **21**.[52,53] Reproduced from ref. 52,53 with permission of Royal Society of Chemistry 2016 and Elsevier 2018.

4.2. PFTB-containing amino acids, peptides and proteins

Monitoring peptides and proteins with imaging technologies is crucial for understanding biological processes and developing diagnostic and therapeutic agents. Thus, introducing fluorinated amino acids (AAs) or tags into peptides and proteins and thus monitoring them with ^{19}F NMR/MRI has become a desirable strategy.[57–59] Notably, besides providing reporter groups for ^{19}F MRI/NMR studies of peptides and proteins dynamics, fluorinated AAs usually enhance the chemical, thermal, and proteolytic stability, modify the folding profile, and impact the biological activity.[60–62]

Compared to extensive studies on monofluorinated, *gem*-difluorinated, and trifluoromethylated AAs since the 1970s, there had been no report on PFTB–AAs until Yu and Jiang reported the synthesis and application of $PFTB_2$-β-AA **24** in 2007 (Fig. 4).[63] With high hydrophobicity and ^{19}F NMR sensitivity, $PFTB_2$-β-AA **24** was developed as a ^{19}F MRI reporter and pharmacokinetic modulator for peptidic pharmaceuticals. As mentioned in the case of PFTB-bioactive agents, it is challenging to generate ^{19}F MRI with PFTB-peptides in biological systems, while the low concentration PFTB-peptides may still facilitate ^{19}F NMR study. (1) PFTB–AAs are sensitive ^{19}F NMR probes to monitor the target binding. L-O-PFTB-homoserine **25** (Fig. 4) was synthesized by Marsh *et al.* as a ^{19}F NMR probe for antimicrobial peptide MSI-78.[64] After incorporating **25** into the 1-, 6-, and 7-position of MSI-78, the resulting PFTB-peptides gave chemical shift changes ($\Delta\delta$ up to 0.41 ppm) and a significant increase of R_2 ($1/T_2$, up to 8.5 times) upon binding to bicelles, which was monitored by ^{19}F NMR at 5 μM with 128 scans. L-O-PFTB-homoserine **25** was also incorporated into the α-helical LXXLL short linear motif of estrogen receptor (ER) coactivator peptides by Zondlo *et al.*[65] The PFTB-peptides exhibited high bioactivity and the process of binding was monitored by ^{19}F NMR. (2) PFTB–AAs are valuable conformational modifiers and probes for peptides and proteins. Zondlo *et al.* synthesized (2*S*,4*R*)-PFTB-4-hydroxyproline **26** and (2*S*,4*S*)-PFTB-4-hydroxyproline **27** (Fig. 4) and incorporated them into α-helical and polyproline helix peptides.[66,67] The conformational species showed distinct conformational preferences and ^{19}F NMR peaks ($\Delta\delta \approx 0.1$ ppm), which were sensitively detected by ^{19}F NMR within 5 min at 200 nM (Scheme 4a and b).[67] Recently, **26** and **27** were employed as sensitive conformational responsive ^{19}F NMR probes for real-time and quantitative monitoring of the phosphorylation process of protein kinases PKA in HeLa cell extracts (Scheme 4c).[68] Notably, not all isomers of PFTB-peptides would give different ^{19}F NMR peaks. For example, Zondlo *et al.* synthesized PFTB-tyrosine **28** and incorporated it into a tetrapeptide, and it was observed that the *cis*- and *trans*-rotamers of the peptide gave identical ^{19}F signals (Fig. 4).[69]

$PFTB_5$-peptide **29** was recently developed by Jiang *et al.* as an "add-on" module to turn regular liposomes into fluorescence (FL) and ^{19}F MRI dual imaging-traceable theranostics (Fig. 4).[70] Peptide **29** had relatively short ^{19}F relaxation times (T_1 542 ms, T_2 152 ms) and was imaged by ^{19}F MRI at 0.11 mM (Fig. 5a), which showed much higher ^{19}F MRI sensitivity than the **3**-labeled lysine counterpart with a detectable concentration of 0.33 mM under the same conditions.[24] Peptide **29** contained 5 pseudo-symmetrical PFTB-groups, which emitted a single ^{19}F peak in methanol, but multiple close peaks in water and 2 close peaks after self-assembly onto the doxorubicin (DOX)-loaded liposome (**L1**, Fig. 5b). The signal splitting indicated that the 5 PFTB-groups were homogeneous in organic solvents and heterogeneous in water after the self-assembly because they had pretty different distances to the hydrophilic PEG terminal and thus different hydrophilic–hydrophobic environments in the self-assembled nanoparticles. Liposome **L1** had a diameter of 70.6 nm and thermo-responsive drug release property (Fig. 5c–e). In liver cancer HepG2 cell xenograft nude mice, liposome **L1** showed improved therapeutic efficacy compared to doxorubicin and gave FL/^{19}F MRI dual imaging for *in vivo* drug tracking. In this case, triple enrichment of $^{19}F_{eff}$ facilitated *in vivo* ^{19}F MRI: (1) integrating 54 pseudo-symmetric ^{19}F into peptide **29**, (2) self-assembly of multiple **29**

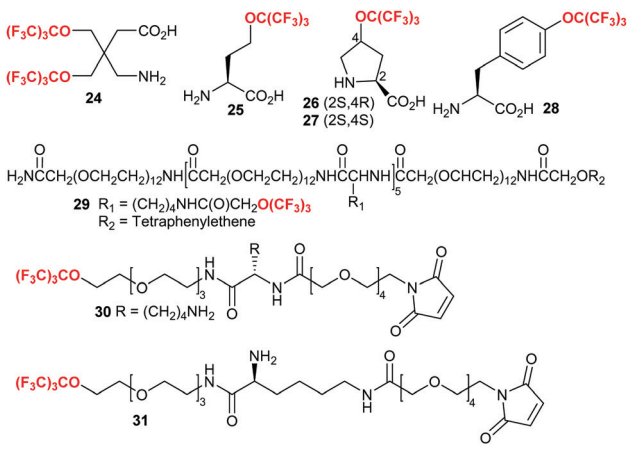

Fig. 4 Structures of PFTB-amino acids, peptides, and tags.

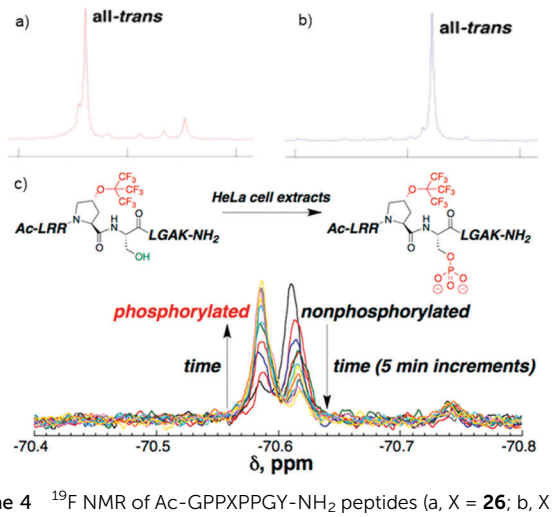

Scheme 4 ^{19}F NMR of Ac-GPPXPPGY-NH_2 peptides (a, X = **26**; b, X = **27**), and time-dependent ^{19}F NMR detection of PKA activity in HeLa cell extracts (c).[67,68] Reproduced from ref. 67 licensed by CC-BY and ref. 68 with permission of American Chemical Society 2020.

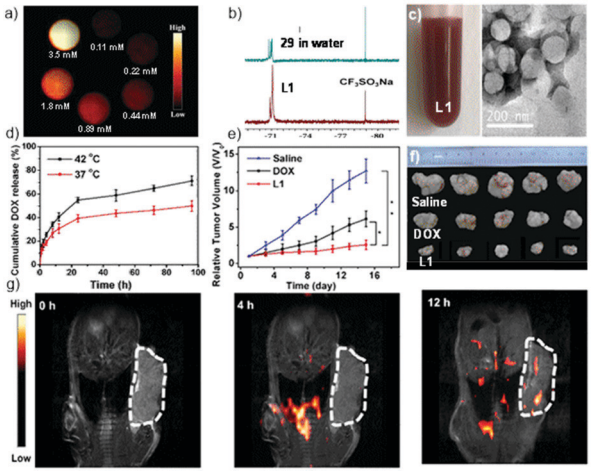

Fig. 5 ^{19}F MRI phantom images (a) and ^{19}F NMR (b, upper in water, lower in **L1**) of peptide **29**, photo and TEM image (c) and thermo-responsive drug release of **L1** (d), tumor growth curve (e), collected tumors at the end of the study (f) and ^{19}F MRI (g) of liposome **L1** treated mice.[70] Reproduced from ref. 70 with permission of Wiley 2019.

onto liposome **L1**, and (3) targeted delivery of liposome **L1** to the tumor region.

Labeling proteins with PFTB-tags may facilitate their ^{19}F NMR study in biological systems. In 2013, Bruce *et al.* developed PFTB-tags **30** and **31** for labeling albumin through Cys-34 (Fig. 4).[71] PFTB-albumin showed dramatically shortened T_1 compared to PFTB-β-mercaptoethanol adducts (from 1520 ms to 630 ms for **30**, from 1470 ms to 680 ms for **31**), while the T_2 of PFTB-albumin was too short to be measured. Although long and flexible linkers between PFTB and albumin were employed, PFTB-albumin gave 2 ^{19}F NMR peaks, which was attributed to the conjugation-induced diastereoisomer formation according to the authors. Because albumin can bind hydrophobic molecules, the signal splitting may be attributed to "free and bound" PFTB-tags. Actually, monitoring PFTB-proteins with ^{19}F NMR is also very difficult. First, it is difficult to achieve sensitive ^{19}F NMR by PFTB-labelling without changing protein bioactivity, solubility, high order structures, *etc.* Second, the large sizes of PFTB-proteins would dramatically shorten their T_2 and thus hamper ^{19}F NMR detection.

4.3. PFTB-containing polymers

Polymerizing fluorinated monomers into polymeric ^{19}F MRI agents is a convenient way to assemble many $^{19}F_{eff}$ without step-by-step synthesis. Although various fluorinated polymers, such as polyvinyl fluoride (PVF), polytetrafluoroethylene (PTFE), and polyvinylidene fluoride (PVDF), have been widely used as high-performance materials, they are not fit for ^{19}F MRI because they are water-insoluble solids with very short T_2. So, polymeric ^{19}F MRI agents should have suitable physicochemical properties, such as liquid with proper T_2, convenient formulation or water-soluble, *etc.* Recently, many fluorinated polymers have been developed for ^{19}F MRI.[72–75] As far as we know, the first PFTB-polymers **32** and **33** were prepared by Riotman and Pittman for the wetting property study in 1972

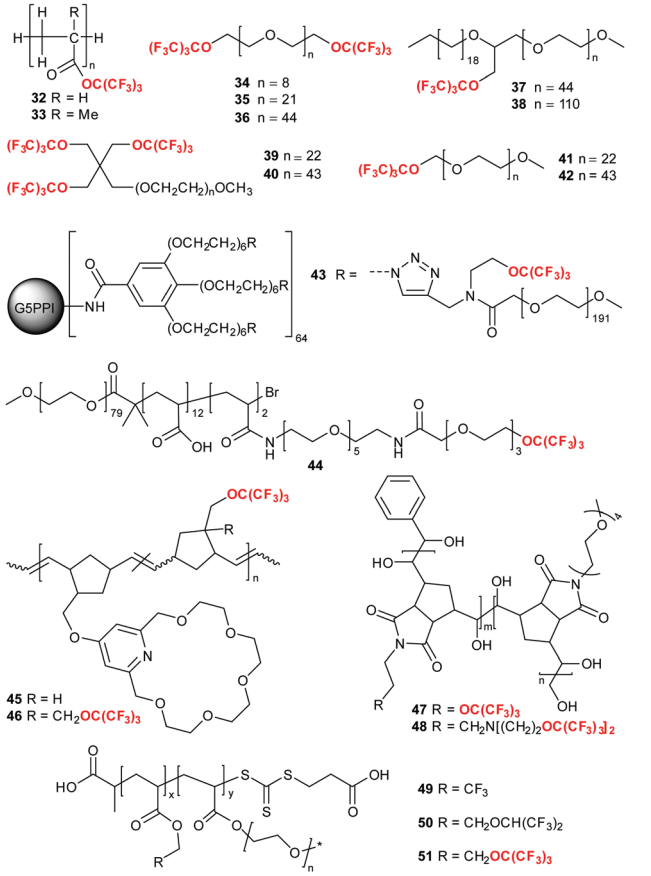

Fig. 6 Structures of PFTB-polymers.

(Fig. 6),[76] while they were amorphous solids and not fit for ^{19}F MRI.

Polyethylene glycols (PEGs) are water-soluble and biocompatible polymers, which are extensively used in biomedicine.[77,78] Modifying PEGs with **PFTB** may be a convenient strategy for water-soluble and biocompatible ^{19}F MRI agents. In 2013, Benaglia *et al.* synthesized $PFTB_2$-PEGs **34–36** and identified **35** as readily available and low-cost ^{19}F MRI agents (Fig. 6).[79] Interestingly, agent **36** with the lowest ^{19}F% was not detectable by ^{19}F MRI in water, in which the ^{19}F%-controlled self-assembly may play a role.[80] Notably, these $PFTB_2$–PEGs are polydisperse mixtures, which may lead to difficulties in purification, characterization, accurate quantification, *etc.* These issues were avoided by using monodisperse PEGs.[23]

PFTB–amphiphilic polymers are attractive self-assembled ^{19}F MRI-traceable drug delivery vehicles. In 2014, Mecozzi *et al.* prepared PFTB–PEGs miktoarm amphiphiles **37** and **38** (Fig. 6).[81] In contrast to their linear perfluoroalkylated amphiphilic counterparts, amphiphiles **37** and **38** aggregated with less kinetic stability and a low paclitaxel loading capability of 1%, probably due to the weak interactions of PFTB-groups. A later study showed that $PFTB_3$-PEGs **39** and **40** formed much more stable and monodisperse sevoflurane-loaded emulsions than PFTB–PEGs **41** and **42** due to the increased entanglement of $PFTB_3$-groups (Fig. 6).[37] With favorable magnetic resonance properties (T_1 530 ms, T_2 110 ms; detected by ^{19}F MRI at 1 mM)

and drug encapsulation capability, PFTB–PEGs **39** may find application in ^{19}F MRI-traceable drug delivery. Notably, in the aggregates, the ^{19}F of 39 and 40 showed higher mobility than the ^{19}F of a control amphiphile $CF_3(CF_2)_5(CH_2CH_2O)_{22}Me$, which promoted high ^{19}F NMR signal intensity. The high mobility of the PFTB-group is crucial for the rational design of NP-based ^{19}F MRI agents, which was further illustrated by a diffusion study on self-assembled dendrimer **43** and polymer **44** with PFTB-groups as ^{19}F NMR diffusion labels (Fig. 6).[82–84] In the self-assembled NPs, the relatively short spacer in **43** and **44** compromised the ^{19}F NMR detection by reducing rotational mobility and severely shortening the T_2.

The host–guest interaction between crown ethers and amines may be useful in drug delivery. For example, Tuba *et al.* synthesized PFTB-copolymers **45** and **46** as hosts to complex amine-containing anti-inflammatory drug Mesalazine (Fig. 6).[85,86] The complex exhibited a pH-responsive drug release profile, which may enable ^{19}F MRI-traceable targeted and sustained drug delivery for the inflamed lower gastrointestinal tract. To improve the water solubility, Kilbinger *et al.* developed water-soluble copolymers **47** and **48** for ^{19}F MRI through dihydroxylation of the olefin bonds, introduction of long and water-soluble linkers, or quaternization of the tertiary amines (Fig. 6),[87] which also improved ^{19}F NMR signal-to-noise ratios (SNRs) by enhancing the rotational mobility of the PFTB-groups.

Measurement of local partial pressure of oxygen (pO_2) is essential for pathological studies and better disease treatment. As a paramagnetic biomarker, oxygen has a notable impact on the T_1 of ^{19}F, *i.e.*, the higher the local pO_2, the shorter the T_1 of ^{19}F.[88] In 2020, Leibfarth *et al.* developed water-soluble fluorinated copolymers **49–51** as oxygen-sensitive ^{19}F MRI agents (Fig. 6).[89] Among the copolymers, PFTB-copolymers **51** showed a high ^{19}F MRI sensitivity of 220 mM and the highest pO_2 sensitivity of 240 × 10^{-5} $mmHg^{-1}$ s^{-1} (Fig. 7a–d). Furthermore, increasing the PFTB-monomer contents in copolymers **51** further increased the pO_2 sensitivity (Fig. 7d).

4.4. PFTB-containing dendrimers

Dendrimers are valuable scaffolds for high-performance ^{19}F MRI agents. (1) Dendrimers contain many symmetrical and pseudo symmetrical positions, which are ideal for assembling multiple $^{19}F_{eff}$ for sensitive ^{19}F MRI. For example, Jiang *et al.* developed a dendritic ^{19}F MRI agent with 540 pseudo-symmetrical ^{19}F from building block **2**, which generated ^{19}F MRI at unprecedented 18.5 μM.[26] **PFTB** is a valuable building block for dendritic ^{19}F MRI agents, from which Yu *et al.* conveniently prepared $PFTB_3$-oils **52–54** and surfactants **55–58** as potential ^{19}F MRI agents (Fig. 8).[21] Based on this work, $PFTB_4$–dendrimer **59** was prepared by Resnati *et al.* (Fig. 8).[40] Recently, a proportionate branching strategy was developed for a defect-free $PFTB_{27}$–dendrimer **60**, which had 243 equivalent ^{19}F from 27 PFTB groups and emitted a sharp ^{19}F peak (Fig. 8).[90] (2) Compared to polymers, dendrimers have accurate structures and their properties can be quantitatively fine-tuned by precise structure modification. With 4 generations of

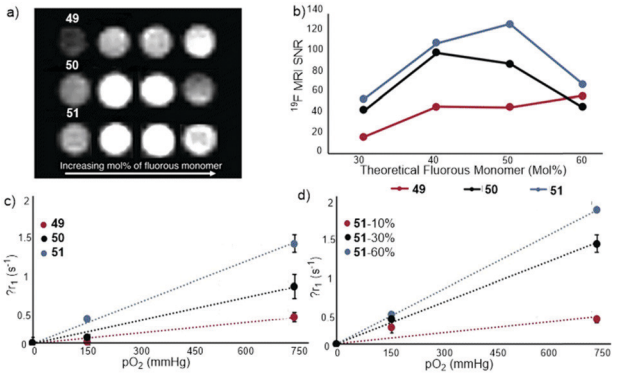

Fig. 7 ^{19}F MRI phantom images (a) and SNR (b) of copolymers **49–51**, plot of Δr_1 *versus* pO_2 of **49–51** (c) and **51** with 10–60% fluorinated monomer contents (d).[89] Reproduced from ref. 89 with permission of Wiley 2020.

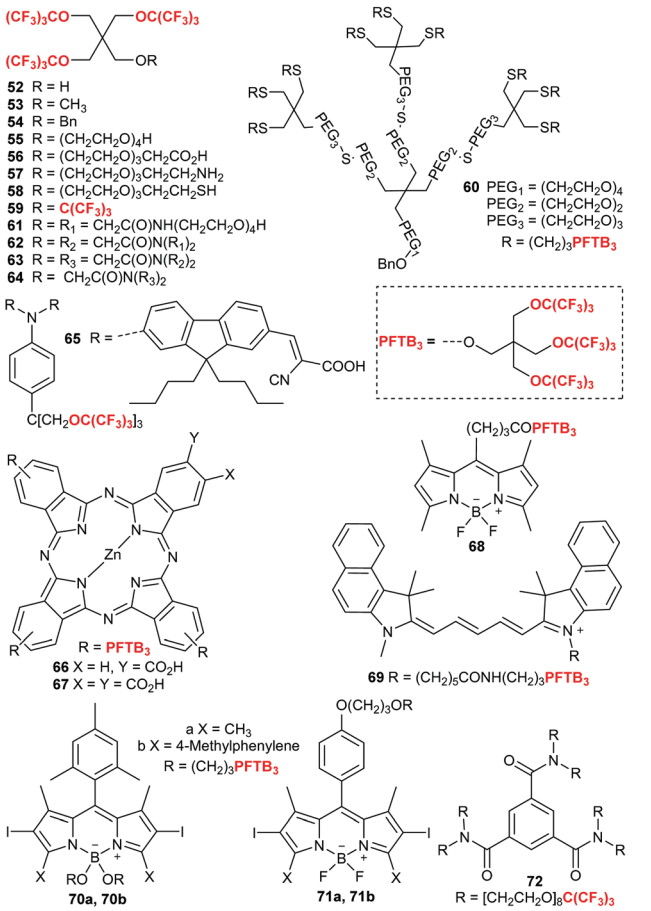

Fig. 8 Structures of **PFTB**–dendrimers and **PFTB**–dendron-fluorophores.

PEG-dendrons as biocompatibility and solubility enhancers, $PFTB_3$–dendrimers **61–64** were efficiently synthesized through a fluorous mixture synthesis (Fig. 8).[91] The physicochemical properties of dendrimers **61–64** were accurately manipulated, from which dendrimer **63** with high ^{19}F MRI sensitivity, biocompatibility and water solubility was identified as a stable and rapidly excreted ^{19}F MRI tracer (Fig. 9).[44] Dendrimer **63** is also a valuable ^{19}F MRI

kinetic probe to obtain the kinetics in major organs with fairly high spatial and temporal resolution.[92] (3) Dendrimers have peculiar 3D structures. Unlike most amphiphiles, dendrimer **73** undergoes intramolecular conformational transition instead of self-association at high concentrations (Fig. 9),[93–95] which may be useful for ^{19}F MRI-traceable concentration-triggered drug release.

Introducing $PFTB_3$-dendrons into fluorophores can provide complementary dual imaging agents with highly sensitive FL imaging and tissue depth limit-free ^{19}F MRI, but also reduce the aggregation tendency and significantly improve the FL performance. Among the $PFTB_3$-fluorophores **65–71b** (Fig. 8),[96–101] $PFTB_3$-BODIPY **68** was employed as a ^{19}F MRI/FL dual imaging agent in a mouse *post-mortem*.[98] It was found that the π–π stacking in BODIPY **70a** was completely avoided by the bulky $PFTB_3$-groups.[100] Although these $PFTB_3$-fluorophores have dual imaging capability, their relatively long relaxation times and poor water solubility severely limited their *in vivo* application.

PEGylation of PFTB–dendrimers can significantly improve their solubility and biocompatibility.[21,26,38,91] Recently, Jiang *et al.* developed a reductive dimerization strategy for efficient preparation of $PFTB_6$–dendrimer **72** as a promising ^{19}F MRI agent (Fig. 8).[102] With 54 $^{19}F_{eff}$ and 6 octaethylene glycol moieties, dendrimer **72** is highly ^{19}F MRI sensitive, water-soluble, biocompatible, and capable of self-assembly into highly monodisperse NPs (Fig. 10).

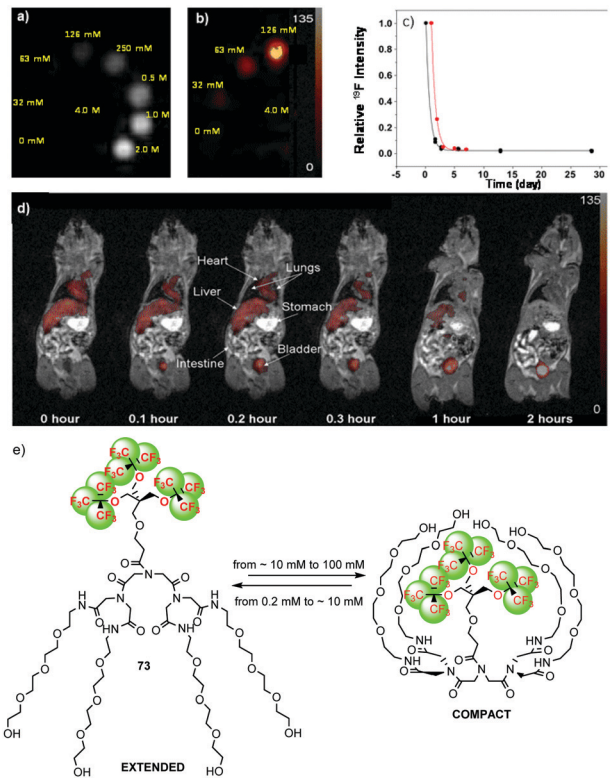

Fig. 9 ^{19}F MRI phantom images (a), ^{19}F NMR signal intensity decay in mice with time (b), and ^{19}F MRI images (c) of dendrimer **63** in mice, and pictorial illustration of concentration-dependent conformation changes of PFTB–dendrimer **73** (e).[44,93] Reproduced from ref. 44 with permission of Wiley 2009.

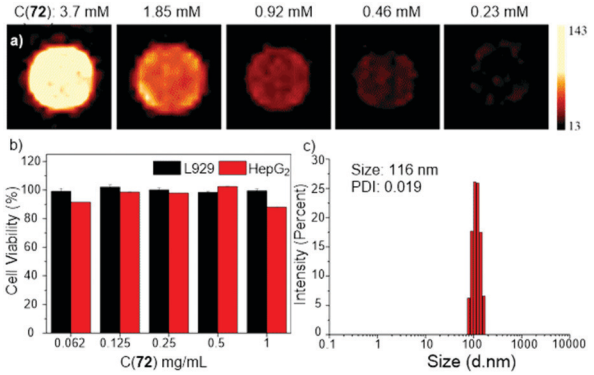

Fig. 10 ^{19}F MRI phantom images (a), biocompatibility assay (b), and dynamic light scattering (c) of $PFTB_6$–dendrimer **72**.[102] Reproduced from ref. 102 with permission of American Chemical Society 2020.

4.5. PFTB-containing nanoparticles

Modifying the NP surface with PFTB-agents or encapsulating PFTB-agents in NPs can conveniently accumulate a large number of $^{19}F_{eff}$ for ^{19}F MRI. The former involves chemical bond formation, while the latter uses physical means. For the former, a notable issue is the ^{19}F signal loss caused by short T_2, which is usually a result of the limited mobility of ^{19}F as previously mentioned.[103] The limited mobility of ^{19}F in PFTB–NPs may be caused by the short or rigid linker of PFTB-groups, tight packing of PFTB-groups, large NP size, *etc.* Thus, delicate PFTB-agents and NP design is crucial for PFTB–NP-based ^{19}F MRI agents. Many PFTB–NPs have been developed, which can be categorized into the following four categories.

4.5.1. Soft NPs with a PFTB-core. Encapsulation of water-insoluble PFTB-agents in NPs with polymers or phospholipids is a convenient strategy for emulsion and micelle-based ^{19}F MRI agents. (1) $PFTB_4$–dendrimer **59** was formulated with lecithin into stable and highly ^{19}F MRI sensitive nanoemulsion (d = 215 nm),[40] which effectively labelled dendritic cells (DCs) with a ^{19}F MRI detection threshold of 9–10 × 10^3 DCs per voxel. In mice, 2 × 10^6 DCs were sensitively tracked by ^{19}F MRI with a data collection time of 10 min. Recently, $PFTB_3$-dendron **10**, ligand **74** and BODIPY were formulated with lecithin into paramagnetic nanoemulsion (d = 195 nm) for sensitively tracking RAW264.7 cells with ^{19}F MRI/FL dual imaging (Fig. 11a–c).[104] The ^{19}F MRI sensitivity was improved by unifying the ^{19}F signals of **10** and **74** with the same $PFTB_3$-dendron and reducing the relaxation times by the ligand **74**-Fe^{3+} complex. (2) $PFTB_4$–dendrimer **59** was co-assembled with fluorinated PEG, $CF_3(CF_2)_{12}CH_2O(CH_2CH_2O)_{44}Me$, into micelles ($d$ = 20 nm) for sensitive tumor detection, which showed high biocompatibility, stability, and ^{19}F MRI sensitivity.[105] In colon cancer mice, about 3.6% of the micelles were detected and quantified in the tumor region by ^{19}F MRI. (3) $PFTB_3$-cyanine **69** was formulated into polymeric NPs (d = 130 nm) with poly(lactic-*co*-glycolic acid) (PLGA) as a ^{19}F MRI/FL dual imaging agent.[101] The polymeric NPs were employed to label and quantify mesenchymal stem cells (MSCs) with ^{19}F MRI/FL dual imaging. The labelled MSCs were quantitatively tracked with dual imaging in mice and monitored with ^{19}F MRI in a traumatic

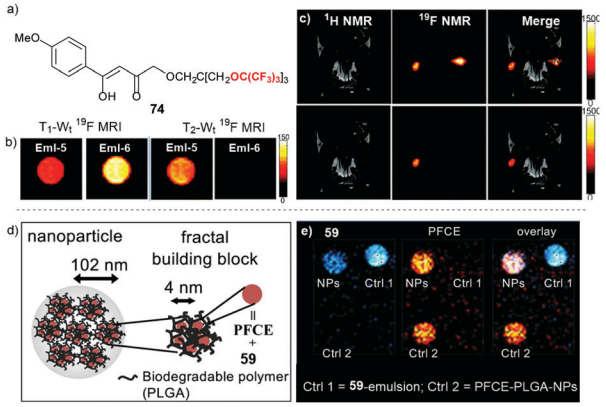

Fig. 11 Structure of $PFTB_3$-ligand **74** (a), T_1/T_2-weighted ^{19}F MRI phantom images (b) and mouse images (c, subcutaneously injected with $PFTB_3$-NP-labelled RAW264.7 cells, left without Fe^{3+} (Eml-5), right with Fe^{3+} (Eml-6), upper T_1-weighted, lower T_2-weighted); structure of the fractal PLGA-NPs (d) and their selective excitation "two color" ^{19}F MRI (e).[104,106] Reproduced from ref. 104 with permission of Royal Society of Chemistry 2018 and ref. 106 licensed by CC-BY.

brain injured (TBI) mouse model. (4) **PFCE** and $PFTB_4$–dendrimer **59** was formulated with PLGA into polymeric NPs with a fractal structure (d = 200 nm),[106] which generated "two-colour" ^{19}F MRI through a chemical shift selective excitation strategy and facilitated simultaneous tracking of 2 targets with ^{19}F MRI (Fig. 11d and e).

4.5.2. Soft NPs with PFTB-surface. To simplify the development of multifunctional NPs, PFTB-amphiphiles **75–78** were developed by Jiang *et al.* as convenient "add-on" modules (Fig. 12a),[107–110] which self-assembled onto the surface of emulsions or liposomes and provided them with ^{19}F MRI, ^{129}Xe hyper CEST, FL, and photodynamic therapy (PDT) capabilities. Modules **75–78** contain $PFTB_3$-dendrons as the ^{19}F signal source, M-PEG-dendrons as the biocompatibility and solubility enhancer, and a functional core. (1) Module **75** with a trimesic acid core was self-assembled onto the doxorubicin (DOX)-loaded liposome, turning it into a ^{19}F MRI-traceable theranostic agent,[107] which was sensitively detected by ^{19}F MRI at 10 μM DOX, corresponding to 5 mM ^{19}F. The PFTB-theranostics enabled the first *in vivo* ^{19}F MRI tracking of anticancer drugs at a therapeutic dose. (2) Module **76** with a BODIPY core was emulsified with perfluorohexane into multifunctional theranostics for ^{19}F MRI/near infrared (NIR)/photoacoustic (PA)-guided cancer PDT.[108] The fluorous interaction between module **76** and perfluorohexane significantly improved the photodynamic effect and NIR capability by relieving the aggregation-induced self-quenching of BODIPY. Notably, tumor hypoxia was also relieved by the oxygen delivery capability of the fluorinated NP. (3) Modules **77** and **78** were employed to encapsulate $PFTB_3$-dendron **10** as multimodal imaging and PDT nanoemulsion.[109,110] To improve the ^{19}F MRI sensitivity, modules **77** and **78**, and dendron **10** contained the same $PFTB_3$-dendron and emitted a unified ^{19}F signal. In this case, multiple "add-on" modules provide the NP with multiple functions besides ^{19}F MRI: module **77** with a cryptophane-A core for highly sensitive ^{129}Xe hyper-CEST MRI and module **78** with a porphyrin core for FL and

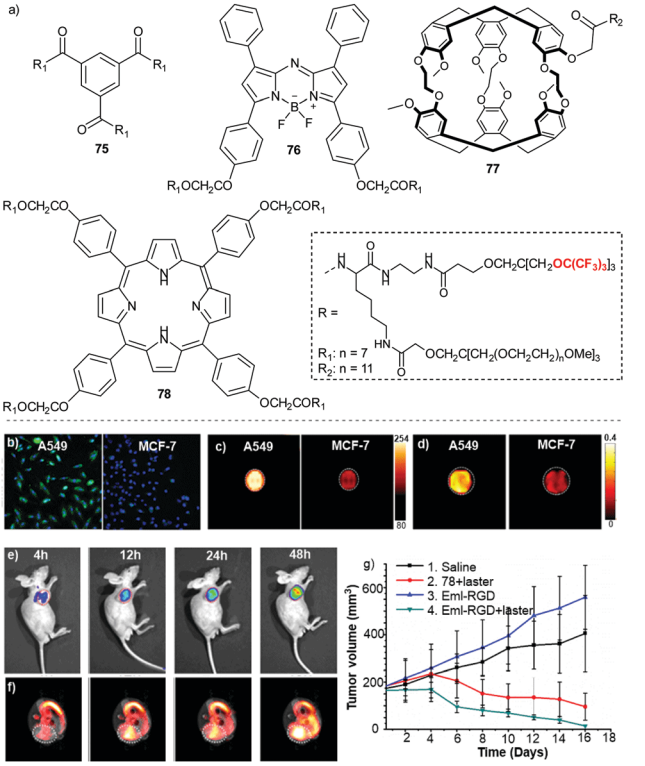

Fig. 12 Structures of "add-on" modules **75–78** (a), FL (b), ^{19}F MRI (c), and ^{129}Xe hyper CEST MRI (d) images of Eml-RGD-treated A549 cells and MCF-7 cells, *in vivo* FL (e) and tumor ^{19}F MRI (f) of Eml-RGD-treated A549 tumor mice, and tumor growth graph of A549 tumor mice after treatments (g).[109] Reproduced from ref. 109 with permission of Royal Society of Chemistry 2020.

PDT. After further surface modification with the c(RGDyC) peptide, the NP (Eml-RGD) became a ^{19}F MRI/^{129}Xe hyper-CEST MRI/FL multimodal imaging-guided and tumor-targeted highly efficient PDT theranostic agent in xenograft A549 tumor mice (Fig. 12b–g). In these cases, the high $^{19}F_{eff}$ in modules **75–78**, the unified ^{19}F frequency, and the high mobility of ^{19}F in the NPs facilitated their high ^{19}F MRI sensitivity.

4.5.3. PFTB–silica-based hard NPs. Compared to PFTB-modified soft NPs, PFTB–silica NPs are more stable and much easier to functionalize on the surface. PFTB-agents can be either encapsulated in the hollow core or attached on the surface. (1) When encapsulated with multiple agents of distinct ^{19}F frequencies, the silica NPs became precious "multicolour" ^{19}F MRI agents for simultaneously monitoring multiple targets with ^{19}F MRI. In 2018, Kikuchi *et al.* encapsulated **PFCE**, $PFTB_3$-dendron **10**, and **TFTBA** in silica NPs (about 140 nm), which have quite different ^{19}F frequencies and thus generated "3-colour" ^{19}F MRI through ^{19}F frequency selective excitation (Fig. 13a).[111] After further functionalization of the surface with PEGs, carboxylic acid and hydroxyl group, respectively, a comparative study on hepatic uptake of the 3 types of silica NPs in mice was monitored with quantitative 3-color ^{19}F MRI, which showed the lowest uptake of PEGylated **PFCE** silica NPs in the liver (Fig. 13b). (2) For ultra-small silica NPs, the surface can be modified with PFTB-groups for ^{19}F MRI. Zhou *et al.* recently

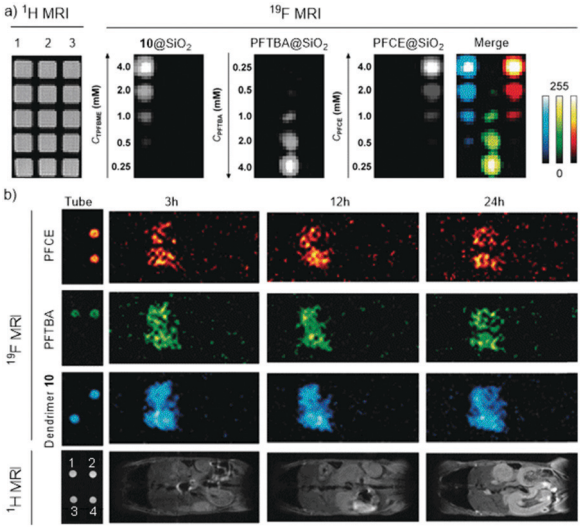

Fig. 13 Multicolor ^{19}F MRI phantom images of silica NPs encapsulated with PFTB$_3$-dendron **10** (left column), **PFTBA** (middle column), and **PFCE** (right column, a), multicolor ^{19}F MRI monitoring of hepatic uptake of silica NPs with different surface modification (b).[111] Reproduced from ref. 111 with permission of Wiley 2018.

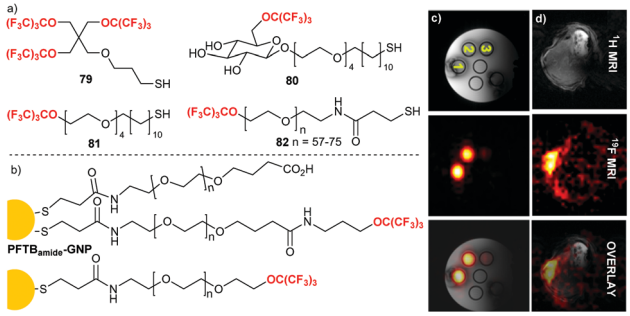

Fig. 14 Structures of PFTB–thiols **79–82** (a) and PFTB–GNP (b), ^{19}F MRI phantom images of PFTB$_{ether}$-GNP (c, ^{19}F concentration for 1–3: 21 mM, 15 mM, 1.5 mM) and images of mouse's belly after i.v. injection of PFTB$_{ether}$-GNP (d).[115] Reproduced from ref. 115 with permission of American Chemical Society 2020.

developed water-soluble and biocompatible PFTB–silica NPs with PFTB-groups directly attached on the surface.[112] Due to the small size of about 5.37 nm, the high mobility of ^{19}F was retained for high ^{19}F signal intensity while the quantum effects of small NPs facilitated label-free blue FL. Further surface modification with the c(RGDyC) peptide enabled ^{19}F MRI/FL dual imaging detection of A549 cells *in vitro* and in xenograft tumor mice.

4.5.4. PFTB–gold-based hard NPs. Surface modification with fluorinated agents is a convenient way to develop gold nanoparticles (GNPs) with ^{19}F MRI, optical and photothermal capabilities. However, the particle size, length of the linker, and compactness of ^{19}F-groups have significant impact on the ^{19}F MRI capability, *i.e.*, larger particle size, shorter linker, and compact ^{19}F weaken or even quench the ^{19}F signal. PFTB–thiols **79–82** with flexible and hydrophilic linkers are favourable agents for developing PFTB–GNP ^{19}F MRI agents (Fig. 14a). (1) PFTB$_3$-dendron **79** was used to modify ultra-small GNPs (d = 1.1 nm) by Metrangolo *et al.*, which provided PFTB$_3$-GNP with a major ^{19}F NMR peak and NIR luminescence at 1050 nm.[113] In this case, the ultra-small GNP facilitated the mobility of ^{19}F (T_1 760 ms; T_2 95 ms) even though a short linker was used. However, the PFTB$_3$-GNP was not water-soluble. (2) To prepare water-soluble PFTB–GNPs, PFTB–thiols **80–82** with hydrophilic linkers were employed to modify small GNPs (d = 2–4 nm) by Carril *et al.* (Fig. 14a).[114] It was found that the long and flexible PEG linker (3000 Da) in the thiol **82**-modified GNP (PFTB$_{ether}$-GNP) facilitated high water-solubility, stability, and ^{19}F MRI sensitivity, while the short linker (176 Da) in the agent **81**-modified GNP led to low stability and a 60% loss of the ^{19}F signal. Recently, Carril *et al.* prepared water-soluble and stable ultra-small PFTB$_{amide}$-GNP (r_c = 1.54 ± 0.54 nm) by first modifying the GNP with a thiol and carboxyl ending PEG ligand and then conjugating part of the carboxyl groups with PFTB-amines (Fig. 14b).[115] Compared to PFTB$_{amide}$-GNP, the long and flexible PEG linker (3000 Da) and the small gold core (r_c = 1.47 ± 0.43 nm) of PFTB$_{ether}$-GNP facilitated high ^{19}F loading (840 ^{19}F per GNP) and high mobility of ^{19}F (T_1 1161 ms, T_2 1030 ms) for sensitive ^{19}F MRI in mice (Fig. 14c and d). Notably, a recent study by Carrillo-Carrión *et al.* showed that modifying the quantum dot surface with PFTB-agents promoted the nanoparticle–cell membrane interactions and cellular uptake.[116] Therefore, PFTB–GNP may find application in cell tracking with ^{19}F MRI/FL dual imaging.

4.6. PFTB-containing chelates

After conjugation of the PFTB-group and the paramagnetic ion chelate through a linker, the paramagnetic ion would significantly affect the chemical shift and relaxation times of ^{19}F through the paramagnetic relaxation enhancement (PRE) effect and pseudo contact shift (PCS) effect. As the distance between the PFTB-group and the paramagnetic ion chelate plays a crucial role in the PER- and PCS-effect, tuning the length, degradability, geometry of the linker, and the redox state of the ion have delivered many valuable ^{19}F MRI agents,[117] which are summarized in the following categories.

4.6.1. PFTB-chelates with fixed linkers. As the macrocyclic chelator DOTA is widely used in ^{1}H MRI, the conjugation of DOTA and **PFTB** may deliver ^{19}F–^{1}H dual MRI agents, multicolor ^{19}F MRI agents, and activatable ^{19}F MRI probes. Yu and Jiang first integrated DOTA and PFTB$_3$-dendron into PFTB$_3$–DOTA **83** and **84** as potential ^{19}F–^{1}H dual MRI agents (Fig. 15a).[118] However their high ^{19}F% (46% and 40%) severely limited the water solubility and hampered further application. After reducing the ^{19}F% to 21%, a water-soluble PFTB–DOTA **85** was developed by Yu and Jiang (Fig. 15a).[119] Upon chelating paramagnetic ions, chelates **85** showed significantly shifted ^{19}F signal frequencies (up to 8 ppm) and environment-insensitive relaxation rates, which may facilitate accurate quantification and simultaneous tracking of multiple targets with "multicolour" ^{19}F MRI (Fig. 15b). Compared to previous "one compound, one colour"-based 3-colour ^{19}F MRI,[111] this "one chelator, multiple colours" strategy is more convenient,

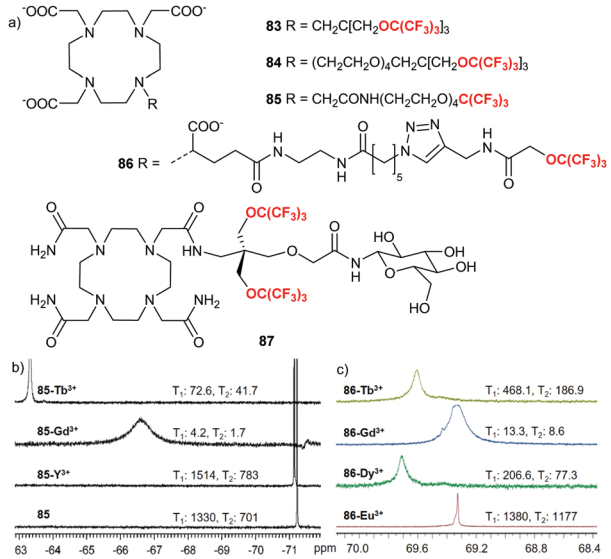

Fig. 15 Structures of PFTB–DOTA **83–87** (a), ^{19}F NMR and relaxation times (in ms) of **85** (b) and **86** (c) chelates.[119,120] Reproduced from ref. 119 with permission of Royal Society of Chemistry 2011 and ref. 120 licensed by CC-BY.

flexible, and reliable, which would be highly valuable for *in vivo* studies due to identical physicochemical and biological properties of the PFTB–DOTA-chelates. In 2020, a similar PFTB–DOTA **86** was developed by Laurent *et al.* as ^{19}F–^{1}H dual MRI agents (Fig. 15a).[120] Compared to chelator **85** containing a tetraethylene glycol linker, chelator **86** with a longer linker had much less changes in the chemical shift and relaxation times, which clearly showed the impact of the linker on the magnetic resonance properties of chelators (Fig. 15c). Molecular dynamic simulations indicated a distance of 4.5 to 10 Å between the ^{19}F and the chelated Gd^{3+}. Recently, Que *et al.* developed water-soluble $PFTB_2$–DOTA **87** as a ^{19}F/^{1}H PARACEST MRI agent, in which a glucose moiety considerably improved the solubility and reduced the ^{19}F% to 29% (Fig. 15).[121] After chelating Fe^{2+}, Co^{2+} and Ni^{2+} with chelator **87**, the PRE-effect significantly reduced the relaxation times, which facilitated highly sensitive ^{19}F MRI detection in the 40–60 μM range as well as ^{1}H PARACEST MRI from the exchangeable amide protons.

4.6.2. PFTB-chelates with variable linkers. Manipulating the distance between the ^{19}F and the paramagnetic ions would considerably attenuate the ^{19}F chemical shift and relaxation times, and this has led to many stimuli-responsive PFTB–DOTA ^{19}F MRI probes. The distance can be manipulated by either enzymatic cleavage of the linker or ion chelating-induced linker conformation changes. (1) Chen *et al.* prepared matrix metalloprotease-2 (MMP-2) activatable ^{19}F MRI probe **88** by conjugating the PFTB-group and Gd^{3+}–DOTA through an MMP-2 cleavable peptide for real-time monitoring of MMP-2 activity (Fig. 16a).[122] The ^{19}F signal of probe **88** was partially turned "off" by the PRE-effect of Gd^{3+}, while it was turned "on" upon MMP-2 cleavage of the linker. While the already pretty long peptidic linker between the ^{19}F and the Gd^{3+} in probe **88** considerably weakened the PRE-effect, a low ^{19}F signal enhancement of 4.8 fold in SCC7 cells was obtained. (2) Recently, Que *et al.* developed PFTB–Tm^{3+}–DO3A **89** as a novel "off to on" ^{19}F MRI probe for Zn^{2+} sensing (Fig. 16a).[123] In this case, the PRE- and PCS-effects of Tm^{3+} turned "off" the ^{19}F signal of probe **89**, while Zn^{2+} chelation increased structural rigidity and reduced the chemical exchange rate, and thus turned "on" the ^{19}F signal (Fig. 16b). (3) Angelovski *et al.* conjugated macrocyclic chelator AAZTA and PFTB-group through a Ca^{2+} chelator EGTA to give a ratiometric ^{19}F MRI probe **90** for Ca^{2+} sensing (Fig. 16c and d).[124] Upon Ca^{2+} chelating, the distance between the ^{19}F and the Dy^{3+} in probe **90** considerably reduced and the ^{19}F signal was reduced accordingly, while diamagnetic Y^{3+} chelated **90** served as a perfect reference. Notably, these stimuli-responsive ^{19}F MRI probes usually suffer from low ^{19}F sensitivity due to low $^{19}F_{eff}$ and solubility. Thus, novel strategies for improving ^{19}F sensitivity, solubility and stimuli-response are of great importance.

4.6.3. PFTB-chelates with variable ion redox states. Besides manipulating the linkers, tuning the redox states of paramagnetic ions in PFTB-chelates is another convenient strategy for stimuli-responsive ^{19}F MRI agents. Following redox state changes, the PRE-effect of paramagnetic ions may be either reduced to turn "on" the ^{19}F signal or enhanced to turn "off" the ^{19}F signal. (1) The redox transition of Co^{2+} to Co^{3+} in PFTB–Co^{2+}-TACN **91** and **92** was accompanied by a significant chemical shift change ($\Delta\delta \approx 10$ ppm) and prolonged T_1, which

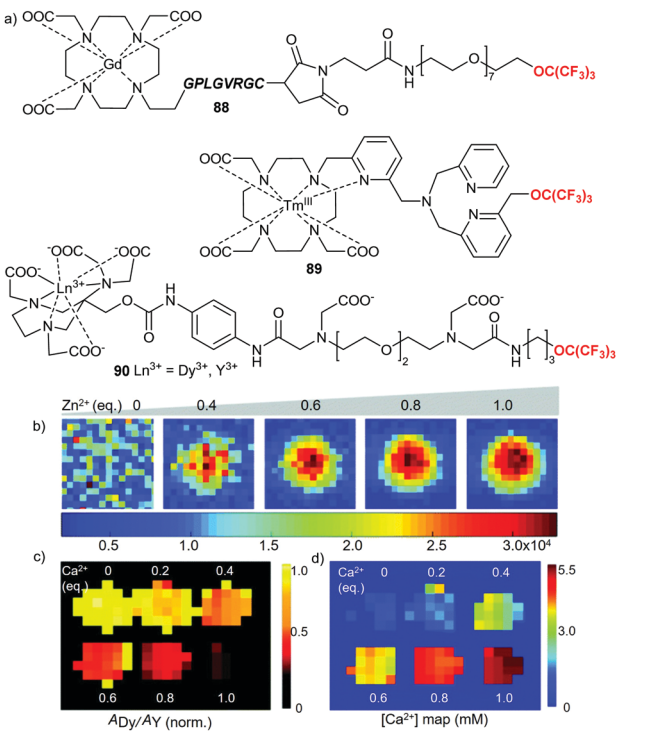

Fig. 16 Structures of PFTB–DOTA **88–90** (a), ^{19}F MRI phantom images of **89** in the presence of Zn^{2+} (b) and **90** chelated with Dy^{3+} and Y^{3+} in the presence of Ca^{2+} (c, normalized Dy^{3+}/Y^{3+} images; d, quantitative Ca^{2+} map).[123,124] Reproduced from ref. 123 with permission of Royal Society of Chemistry 2020 and ref. 124 licensed by CC-BY.

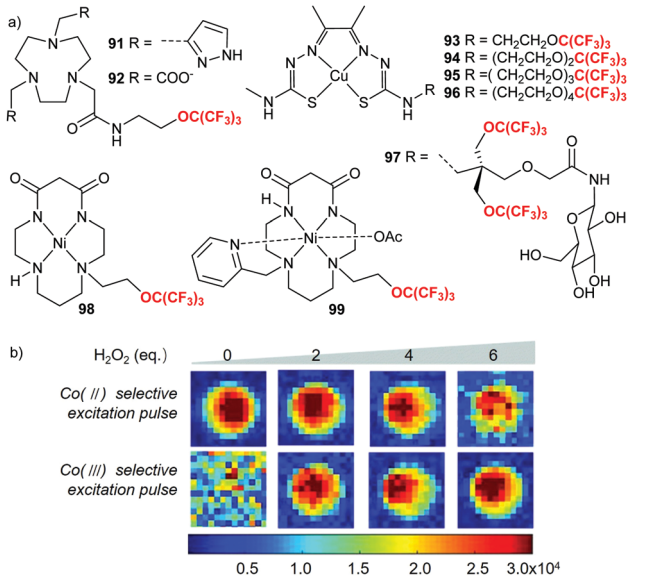

Fig. 17 Structures of PFTB-chelates **91–99** (a), chemical shift selective ^{19}F MRI phantom images of **92** in the presence of H_2O_2 (b).[125] Reproduced from ref. 125 with permission of American Chemical Society 2018.

was employed by Que *et al.* to monitor H_2O_2 production and peroxidase activity with ^{19}F MRI (Fig. 17a and b).[125] The large chemical shift difference facilitated ^{19}F MRI detection of both species through chemical shift selective pulse sequences. (2) The redox transition of paramagnetic Cu^{2+} to diamagnetic Cu^{+} was also employed by Que *et al.* in the development of PFTB–Cu^{2+}-ATSM **93–96** as a reduction agent-responsive ^{19}F MRI/NMR probe (Fig. 17a).[126] Notably, the PEG linker in probes **93–96** played multiple roles and the tetraethylene glycol linker showed better reduction potential, relaxation properties and hydrophilicity. However, probe **96** suffered from low water solubility and ^{19}F sensitivity during an *in vivo* study. Then, probe **97** with 2 PFTB-groups for higher ^{19}F signal intensity and a glucose moiety for better solubility was developed, which was further formulated into nanoemulsion (d = 100 nm) for *in vivo* application (Fig. 17a).[127] (3) The pH-sensitive Ni^{2+} coordination states of diamagnetic chelate **98** and paramagnetic chelate **99** were employed by Que *et al.* to sense pH with chemical shift selective ^{19}F MRI (Fig. 17a).[128]

5. Current status of ^{19}F MRI agents

Compared to ^{1}H MRI agents with extensive clinical application, ^{19}F MRI agents have not gained clinical application even after nearly 50 years' research and development. Up to June 2021, there are only 6 ^{19}F MRI agents in clinical trials, according to the database of www.clinicaltrials.gov (Table 1). **PFP** gas, the most promising ^{19}F MRI agent for clinical application, has passed many phase I clinical trials for ^{19}F MRI diagnosis of various lung diseases and entered the phase II clinical trial for chronic obstructive pulmonary disorder (COPD). **PFPE** and **PFCE**-based emulsions are currently in either preclinical trials or phase I clinical trials for ^{19}F MRI cell tracking-assisted diagnosis and therapy. On the other hand, **HFB** and **PFCE**-filled capsules have been suspended from clinical trials for irritable bowel syndrome due to technical problems.

Table 1 ^{19}F MRI agents in clinical trial

Entry	^{19}F MRI agents	Indications	Phase
1	**PFP** gas	Small airways disease	Phase 1
		Asthma, post lung transplant	
		Lung cancer, cystic fibrosis	
		Constrictive bronchiolitis	
		War lung injury syndrome	
		Emphysema	
		COPD	Phase 2
2	CS-1000 (**PFPE**)	SVF cell tracking	Phase 1
		PBMC tracking	
3	VS-1000 (**PFPE**)	Cell tracking	Preclinical
4	CS-580 (**PFCE**)	Cell tracking	Preclinical
5	VS-580 (**PFCE**)	Cell tracking	Preclinical
6	**HFB**, **PFCE**	Irritable bowel syndrome	Suspended

The considerable gap between the booming ^{19}F MRI research and its poor clinical application indicates many advantages and disadvantages of ^{19}F MRI agents. On the one hand, compared to the commercially available Gd^{3+} and other metal-based ^{1}H MRI agents, ^{19}F MRI agents have many peculiar advantages, including "hot spot" images without background, high specificity, quantitative images, stimuli and environmental sensitivity, relatively high biocompatibility, *etc.*, which would lead to even more application in biomedical research. On the other hand, in contrast to ^{1}H MRI using ubiquitous and abundant water in biological systems as a signal source, ^{19}F MRI employs biologically orthogonal and absent fluorinated agents as signal sources. So, ^{19}F MRI agents suffer from the disadvantages of low sensitivity, high dosage, and safety concerns. The low sensitivity of MRI usually requires lower millimolar local $^{19}F_{eff}$ concentration to generate clear ^{19}F MR images within reasonable data collection time. The high local $^{19}F_{eff}$ concentration may be achievable in many *in vitro* studies but very challenging during *in vivo* studies. The *in vivo* dilution by body fluid and the off-target issue would hamper the ^{19}F MRI detection and require a high dose of the ^{19}F MRI agent, which usually leads to toxicity, severe organ retention, and safety concerns, which may be the main reason why many ^{19}F MRI agents in biomedical research can hardly be translated into clinical application. Although most PFCs have relatively high biocompatibility, the long organ resident time has raised considerable safety concerns. For example, due to the long resident time in humans and the environment, perfluorooctane sulfonic acid (PFOS) and perfluorooctanoic acid (PFOA) have been banned from use by the United Nations (UN).

Recently, many strategies have been developed to address the high dose issue and safety concerns of ^{19}F MRI agents. (1) Many synthetic ^{19}F MRI agents, *e.g.*, PFTB–dendrimer **63**, with high biocompatibility and short organ resident time facilitated the high dose and safe *in vivo* ^{19}F MRI. (2) Many sensitivity enhancing ways, such as unifying the ^{19}F signal, shortening the relaxation times, and assembly or encapsulation of many $^{19}F_{eff}$, considerably reduced the *in vivo* dose of ^{19}F MRI agents. (3) Many *in vivo* enrichment methods, such as nanotechnology,

targeted delivery, and stimuli-responsive techniques, improved the specificity and further reduced the dose of ^{19}F MRI agents. Although extensively used in biomedical research, PFC-based ^{19}F MRI agents would eventually face safety issues. Synthetic ^{19}F MRI agents, *e.g.*, PFTB-agents, have shown obvious advantages over PFC-based ones, such as high sensitivity, and good physicochemical and biological properties. But the case-by-case synthesis and high cost of these synthetic ^{19}F MRI agents are still hampering their clinical application.

6. Conclusion and prospects

In this feature article, we have summarized the prominent roles of **PFTB** in the development and application of various high-performance ^{19}F MRI agents from the angles of chemistry, magnetic resonance, and biomedicine. In the last 15 years, PFTB–^{19}F MRI agents have gained rapid development and significantly promoted ^{19}F MRI in biomedicine. Compared to the PFCs, **PFTB** has shown its bright side of an intense ^{19}F signal from all equivalent ^{19}F and its versatile side of fitting into various needs with an easily modifiable hydroxyl handle, which provides many synthetic means to achieve high sensitivity, solubility, biocompatibility, and multifunctionality. In contrast, modification of PFCs is challenging due to the lack of a modifiable group and the high fluorine content-induced abnormal chemical reactivity (fluorous effect). Thus, PFCs are more fit for developing NP-based ^{19}F MRI agents, while **PFTB** is fit for developing both NP-based and single molecule-based ^{19}F MRI agents. Furthermore, PFTB–^{19}F MRI agents have contributed to solving the critical issues of sensitivity, organ retention, and specificity in PFC-based ^{19}F MRI agents. However, **PFTB** also has its weak side in ^{19}F MRI agent development, such as relying on chemical synthesis, inducing low solubility and aggregation tendency, limited ^{19}F signal response ($\Delta\delta < 1$ ppm) to molecular geometry, microenvironment, and target interactions, *etc.*

The future development, especially potential clinical application, of PFTB–^{19}F MRI agents relies on the multidisciplinary collaboration of chemistry, nanotechnology, biomedicine, and magnetic resonance communities. First, the case-by-case synthesis of PFTB–^{19}F MRI agents is always challenging, time-consuming, and expensive, which severely limits their biomedical application. Thus, it would be beneficial to develop and commercialize some general PFTB-building blocks and multifunctional PFTB-modules, which may significantly relieve the synthetic burden of PFTB–^{19}F MRI agents. Besides the $PFTB_3$-dendron **10** and the ''add-on'' modules **75–78**, more PFTB-modules with easy conjugation and multifunction are preferred, such as ''clickable'', multimodal imaging, and stimuli-responsive modules. Second, incorporating readily available PFTB-modules into NPs and modulating the relaxation times with the EPR effect may efficiently address the sensitivity issue of ^{19}F MRI agents. Encapsulating PFTB-modules, *e.g.*, $PFTB_3$-dendron **10** prepared in 1 step on 30 g scales, into NPs can easily include millions of $^{19}F_{eff}$ in a single NP. However synthetic ^{19}F MRI agents are inferior because the more the $^{19}F_{eff}$ in a molecule the more the synthetic steps required, which significantly increases the cost and limits the availability. For example, $PFTB_{27}$-dendron **60** with 243 $^{19}F_{eff}$ was synthesized in 12 steps with a 9% yield, which can hardly scale up for ^{19}F MRI application. Finally, the development of magnetic resonance hardware, hyperpolarize strategy, and pulse sequence would significantly improve ^{19}F MRI agents' sensitivity and promote their clinical translation. For example, strategies to hyperpolarize ^{19}F would revolutionize the current way of using ^{19}F MRI agents by dramatically reducing their dose and imaging targets at micromolar even nanomolar concentrations. With the development of PFTB–^{19}F MRI agents, ^{19}F MRI will continually be an extremely promising quantification and tracking technology to address critical biomedical issues and beyond.

Conflicts of interest

There are no conflicts to declare.

Acknowledgements

The authors thank the National Natural Science Foundation of China (22077098 and 91859206) and the National Key R&D Program of China (2018YFA0704000).

Notes and references

1 M. T. Vlaardingerbroek and J. A. Boer, *Magnetic resonance imaging*, Springer Science & Business Media, Springer-Verlag Berlin Heidelberg, 2013, vol. 2.
2 R. Weissleder and M. J. Pittet, *Nature*, 2008, **452**, 580–589.
3 P. Caravan, J. J. Ellison, T. J. McMurry and R. B. Lauffer, *Chem. Rev.*, 1999, **99**, 2293–2353.
4 H. Li and T. J. Meade, *J. Am. Chem. Soc.*, 2019, **141**, 17025–17041.
5 Y. B. Yu, *Wiley Interdiscip. Rev.: Nanomed. Nanobiotechnol.*, 2013, **5**, 646–661.
6 R.-C. Jesús, P. B. Brad, P. A. Bottomley and J. W. M. Bulte, *NMR Biomed.*, 2011, **24**, 114–129.
7 I. Tirotta, V. Dichiarante, C. Pigliacelli, G. Cavallo, G. Terraneo, F. B. Bombelli, P. Metrangolo and G. Resnati, *Chem. Rev.*, 2015, **115**, 1106–1129.
8 W. Wolf, C. A. Presant and V. Waluch, *Drug Delivery Rev.*, 2000, **41**, 55–74.
9 C. Han, S. Viel, F. Ziarelli and L. Peng, *Chem. Soc. Rev.*, 2013, **42**, 7971–7982.
10 J. Wang, M. Sánchez-Roselló, J. L. Aceña, C. del Pozo, A. E. Sorochinsky, S. Fustero, V. A. Soloshonok and H. Liu, *Chem. Rev.*, 2014, **114**, 2432–2506.
11 Y. Ogawa, E. Tokunaga, O. Kobayashi, K. Hirai and N. Shibata, *iScience*, 2020, **23**, 101467.
12 R. Berger, G. Resnati, P. Metrangolo, E. Weber and J. Hulliger, *Chem. Soc. Rev.*, 2011, **40**, 3496–3508.
13 G. N. Holland, P. A. Bottomley and W. S. Hinshaw, *J. Magn. Reson.*, 1977, **28**, 133–136.
14 L. S. Li, Y. Li, Y. J. Lan and J. H. Zhang, *Chin. J. Magn. Reson.*, 2007, **24**, 353–364.
15 E. T. Ahrens, R. Flores, H. Xu and P. A. Morel, *Nat. Biotechnol.*, 2005, **23**, 983–987.
16 H. Zhang, S. Chen, Y. Yuan, Y. Li, Z.-X. Jiang and X. Zhou, *ACS Appl. Bio Mater.*, 2019, **2**, 27–32.
17 R. P. Mason, P. P. Antich, E. E. Babcock, J. L. Gerberich and R. L. Nunnally, *Magn. Reson. Imaging*, 1989, **7**, 475–485.
18 U. Flögel, Z. Ding, H. Hardung, S. Jander, G. Reichmann, C. Jacoby, R. Schubert and J. Schrader, *Circulation*, 2008, **118**, 140–148.

19 U. Gross, S. Rudiger and H. Reichelt, *J. Fluorine Chem.*, 1991, **53**, 155–161.
20 Y. Nosé, *Artif. Organs*, 2004, **28**, 807–812.
21 Z.-X. Jiang and Y. B. Yu, *Tetrahedron*, 2007, **63**, 3982–3988.
22 E. Parman, L. Toom, S. Selberg and I. Leito, *J. Phys. Org. Chem.*, 2019, **32**, e3940.
23 Y. Li, B. Thapa, H. Zhang, X. Li, F. Yu, E.-K. Jeong, Z. Yang and Z.-X. Jiang, *Tetrahedron*, 2013, **69**, 9586–9590.
24 J. Zhu, Y. Xiao, H. Zhang, Y. Li, Y. Yuan, Z. Yang, S. Chen, X. Zheng, X. Zhou and Z.-X. Jiang, *Biomacromolecules*, 2019, **20**, 1281–1287.
25 X. Wang, Y. Li, T. Wu, Z. Yang, X. Zheng, S. Chen, X. Zhou and Z.-X. Jiang, *Biomacromolecules*, 2020, **21**, 725–731.
26 W. Yu, Y. Yang, S. Bo, Y. Li, S. Chen, Z. Yang, X. Zheng, Z.-X. Jiang and X. Zhou, *J. Org. Chem.*, 2015, **80**, 4443–4449.
27 S. Bo, C. Song, Y. Li, W. Yu, S. Chen, X. Zhou, Z. Yang, X. Zheng and Z.-X. Jiang, *J. Org. Chem.*, 2015, **80**, 6360–6366.
28 X. Liu, Y. Yuan, S. Bo, Y. Li, Z. Yang, X. Zhou, S. Chen and Z.-X. Jiang, *Eur. J. Org. Chem.*, 2017, 4461–4468.
29 B. L. Dyatkin, E. P. Mochalina and I. L. Knunyants, *Tetrahedron*, 1965, **21**, 2991–2995.
30 R. Filler and R. M. Schure, *J. Org. Chem.*, 1967, **32**, 1217–1219.
31 F. J. Pavlik and P. E. Toren, *J. Org. Chem.*, 1970, **35**, 2054–2056.
32 S. P. Kotun, J. D. O. Anderson and D. D. DesMarteau, *J. Org. Chem.*, 1992, **57**, 1124–1131.
33 D. Szabó, J. Mohl, A.-M. Bálint, A. Bodor and J. Rábai, *J. Fluorine Chem.*, 2006, **127**, 1496–1504.
34 Q. Chu, C. Henry and D. P. Curran, *Org. Lett.*, 2008, **10**, 2453–2456.
35 Z.-X. Jiang, Y. Feng and Y. B. Yu, *Chem. Commun.*, 2011, **47**, 7233–7235.
36 X. Zhao, W. Y. Ng, K.-C. Lau, A. E. C. Collis and I. T. Horváth, *Phys. Chem. Chem. Phys.*, 2012, **14**, 3909–3914.
37 S. Decato, T. Bemis, E. Madsen and S. Mecozzi, *Polym. Chem.*, 2014, **5**, 6461–6471.
38 H. Zhang, X. Li, Q. Shi, Y. Li, G. Xia, L. Chen, Z. Yang and Z.-X. Jiang, *Angew. Chem., Int. Ed.*, 2015, **54**, 3763–3767.
39 J. J. Kasper, J. E. Hitro, S. R. Fitzgerald, J. M. Schnitter, J. J. Rutowski, J. A. Heck and J. L. Steinbacher, *J. Org. Chem.*, 2016, **81**, 8095–8103.
40 I. Tirotta, A. Mastropietro, C. Cordiglieri, L. Gazzera, F. Baggi, G. Baselli, M. G. Bruzzone, I. Zucca, G. Cavallo, G. Terraneo, F. B. Bombelli, P. Metrangolo and G. A. Resnati, *J. Am. Chem. Soc.*, 2014, **136**, 8524–8527.
41 R. J. A. Nabuurs, V. V. Kapoerchan, A. Metaxas, S. de Jongh, M. de Backer, M. M. Welling, W. Jiskoot, A. D. Windhorst, H. S. Overkleeft, M. A. van Buchem, M. Overhand and L. van der Weerd, *Bioorg. Med. Chem.*, 2014, **22**, 2469–2481.
42 C. M. Tressler and N. J. Zondlo, *Org. Lett.*, 2016, **18**, 6240–6243.
43 H. Meng, L. Wen, Z. Xu, Y. Li, J. Hao and Y. Zhao, *Org. Lett.*, 2019, **21**, 5206–5210.
44 Z.-X. Jiang, X. Liu, E.-K. Jeong and Y. B. Yu, *Angew. Chem., Int. Ed.*, 2009, **48**, 4755–4758.
45 W. K. Hagmann, *J. Med. Chem.*, 2008, **51**, 4359–4369.
46 K. Müller, C. Faeh and F. Diederich, *Science*, 2007, **317**, 1881–1886.
47 G. Schitter, A. J. Steiner, G. Pototschnig, E. Scheucher, M. Thonhofer, C. A. Tarling, S. G. Withers, K. Fantur, E. Paschke, D. J. Mahuran, B. A. Rigat, M. B. Tropak, C. Illaszewicz, R. Saf, A. E. Stütz and T. M. Wrodnigg, *ChemBioChem*, 2010, **11**, 2026–2033.
48 T. Snyder-Leiby, S. Dingman, R. Thomas and C. Guo, *Appl. Microbiol. Biotechnol.*, 2004, **64**, 223–227.
49 S. Dingman, T. Snyder-Leiby, D. J. Mack, R. Thomas and C. Guo, *Appl. Microbiol. Biotechnol.*, 2004, **64**, 556–559.
50 S. Orlandi, M. Cavazzini, S. Capuani, A. Ciardello and G. Pozzi, *J. Fluorine Chem.*, 2020, **237**, 109596.
51 K. Tanabe, H. Harada, M. Narazaki, K. Tanaka, K. Inafuku, H. Komatsu, T. Ito, H. Yamada, Y. Chujo, T. Matsuda, M. Hiraoka and S.-i. Nishimoto, *J. Am. Chem. Soc.*, 2009, **131**, 15982–15983.
52 Q. Shi, Y. Li, S. Bo, X. Li, P. Zhao, Q. Liu, Z. Yang, H. Cong, H. Deng, M. Chen, S. Chen, X. Zhou, H. Ding and Z.-X. Jiang, *Chem. Commun.*, 2016, **52**, 5136–5139.
53 Y. Li, Q. Shi, J. Shao, Y. Yuan, Z. Yang, S. Chen, X. Zhou, S. Wen and Z.-X. Jiang, *Eur. J. Med. Chem.*, 2018, **148**, 279–290.
54 H. Shi, B. Lai, S. Chen, X. Zhou, J. Nie and J.-A. Ma, *Chin. J. Chem.*, 2017, **35**, 1693–1700.
55 K. Tanabe, Z. Zhang, T. Ito, H. Hatta and S. Nishimoto, *Org. Biomol. Chem.*, 2007, **5**, 3745–3757.
56 P. B. Gupta, T. T. Onder, G. Jiang, K. Tao, C. Kuperwasser, R. A. Weinberg and E. S. Lander, *Cell*, 2009, **138**, 645–659.
57 E. N. G. Marsh and Y. Suzuki, *ACS Chem. Biol.*, 2014, **9**, 1242–1250.
58 K. E. Arntson and W. C. K. Pomerantz, *J. Med. Chem.*, 2016, **59**, 5158–5171.
59 C. D. Pietrantonio, A. Pandey, J. Gould, A. Hasabnis and R. S. Prosser, *Methods Enzymol.*, 2019, **615**, 103–130.
60 E. N. G. Marsh, *Acc. Chem. Res.*, 2014, **47**, 2878–2886.
61 A. B. Allison, V. Jan-Stefan, B. Nediljko and K. Beate, *Acc. Chem. Res.*, 2017, **50**, 2093–2103.
62 S. Huhmann and B. Koksch, *Eur. J. Org. Chem.*, 2018, 3667–3679.
63 Z.-X. Jiang and Y. B. Yu, *J. Org. Chem.*, 2007, **72**, 1464–1467.
64 B. C. Buer, B. J. Levin and E. N. G. Marsh, *J. Pept. Sci.*, 2013, **19**, 308–314.
65 C. M. Tressler and N. J. Zondlo, *Biochemistry*, 2017, **56**, 1062–1074.
66 A. K. Pandey, D. Naduthambi, K. M. Thomas and N. J. Zondlo, *J. Am. Chem. Soc.*, 2013, **135**, 4333–4363.
67 C. M. Tressler and N. J. Zondlo, *J. Org. Chem.*, 2014, **79**, 5880–5886.
68 C. M. Tressler and N. J. Zondlo, *ACS Chem. Biol.*, 2020, **15**, 1096–1103.
69 C. M. Tressler and N. J. Zondlo, *Org. Lett.*, 2016, **18**, 6240–6243.
70 J. Zhu, H. Zhang, K. Chen, Y. Li, Z. Yang, S. Chen, X. Zheng, X. Zhou and Z.-X. Jiang, *Adv. Healthcare Mater.*, 2020, **9**, 1901331.
71 X. Yue, Y. Feng and Y. B. Yu, *J. Fluorine Chem.*, 2013, **152**, 173–181.
72 E. Gianolio, R. Napolitano, F. Fedeli, F. Arena and S. Aime, *Chem. Commun.*, 2009, 6044–6046.
73 L. Nurmi, H. Peng, J. Seppälä, D. M. Haddleton, I. Blakey and A. K. Whittaker, *Polym. Chem.*, 2010, **1**, 1039–1047.
74 K. J. Thurecht, I. Blakey, H. Peng, O. Squires, S. Hsu, C. Alexander and A. K. Whittaker, *J. Am. Chem. Soc.*, 2010, **132**, 5336–5337.
75 C. Zhang, D. S. Kim, J. Lawrence, C. J. Hawker and A. K. Whittaker, *ACS Macro Lett.*, 2018, **7**, 921–926.
76 J. N. Roitman and A. G. Pittman, *J. Polym. Sci., Part B: Polym. Lett.*, 1972, **10**, 499–503.
77 K. Knop, R. Hoogenboom, D. Fischer and U. S. Schubert, *Angew. Chem., Int. Ed.*, 2010, **49**, 6288–6308.
78 T. Wu, K. Chen, S. He, X. Liu, X. Zheng and Z.-X. Jiang, *Org. Process Res. Dev.*, 2020, **24**, 1364–1372.
79 C. Biaggi, M. Benaglia, M. Ortenzi, E. Micotti, C. Perego and M. G. D. Simoni, *J. Fluorine Chem.*, 2013, **153**, 172–177.
80 S. Rossi, M. Benaglia, M. Ortenzi, E. Micotti, C. Perego and M. G. D. Simoni, *Tetrahedron Lett.*, 2011, **52**, 6581–6583.
81 W. B. Tucker, A. M. McCoy, S. M. Fix, M. F. Stagg, M. M. Murphy and S. Mecozzi, *J. Polym. Sci., Part A: Polym. Chem.*, 2014, **52**, 3324–3336.
82 D. W. De Kort, J. P. M. van Duynhoven, F. J. M. Hoeben, H. M. Janssen and H. Van As, *Anal. Chem.*, 2014, **86**, 9229–9235.
83 D. W. De Kort, W. H. Rombouts, F. J. M. Hoeben, H. M. Janssen, H. Van As and J. P. M. van Duynhoven, *Macromolecules*, 2015, **48**, 7585–7591.
84 N. Bourouina, D. W. de Kort, F. J. M. Hoeben, H. M. Janssen, H. Van As, J. Hohlbein, J. P. M. van Duynhoven and J. M. Kleijn, *Langmuir*, 2015, **31**, 12635–12643.
85 E. Kovacs, J. Deme, G. Turczel, T. Nagy, V. Farkas, L. Trif, S. Keki, P. Huszthy and R. Tuba, *Polym. Chem.*, 2019, **10**, 5626–5634.
86 V. Farkas, G. Turczel, J. Deme, A. Domján, L. Trif, A. Mirzaei, D. Vu Hai, M. Nagyházi, S. Kéki, P. Huszthy and R. Tuba, *Polym. Chem.*, 2021, **12**, 2175–2180.
87 I. K. Tennie and A. F. M. Kilbinger, *Macromolecules*, 2020, **53**, 10386–10396.
88 P. Parhami and B. M. Fung, *J. Phys. Chem.*, 1983, **87**, 1928–1931.
89 N. G. Taylor, S. H. Chung, A. L. Kwansa, R. R. Johnson, A. J. Teator, N. J. B. Milliken, K. M. Koshlap, Y. G. Yingling, Y. Z. Lee and F. Leibfarth, *Chem. – Eur. J.*, 2020, **26**, 9982–9990.
90 X. Yue, M. Taraban, L. L. Hyland and Y. B. Yu, *J. Org. Chem.*, 2012, **77**, 8879–8887.
91 Z.-X. Jiang and Y. B. Yu, *J. Org. Chem.*, 2010, **75**, 2044–2049.
92 X. Liu, Z.-X. Jiang, B. Y. Yu and E.-K. Jeong, *Magn. Reson. Mater. Phys., Biol. Med.*, 2019, **32**, 97–103.

93 M. B. Taraban, Y. Li, F. Yue, E. V. Jouravleva, M. A. Anisimov, Z.-X. Jiang and Y. B. Yu, *RSC Adv.*, 2014, **4**, 54565–54575.
94 M. B. Taraban, D. J. Deredge, M. E. Smith, K. T. Briggs, Y. Li, Z.-X. Jiang, P. L. Wintrode and Y. B. Yu, *Magn. Reson. Chem.*, 2019, **57**, 861–872.
95 M. B. Taraban, D. J. Deredge, M. E. Smith, K. T. Briggs, Y. Feng, Y. Li, Z.-X. Jiang, P. L. Wintrode and Y. B. Yu, *RSC Adv.*, 2019, **9**, 1956–1966.
96 I. Pecnikaj, D. Minudri, L. Otero, F. Fungo, M. Cavazzini, S. Orlandi and G. Pozzi, *New J. Chem.*, 2017, **41**, 7729–7738.
97 G. Pozzi, S. Quici, M. C. Raffo, C. A. Bignozzi, S. Caramori and M. J. Orlandi, *J. Phys. Chem. C*, 2011, **115**, 3777–3788.
98 A. M. Huynh, A. Müller, S. M. Kessler, S. Henrikus, C. Hoffmann, A. K. Kiemer, A. Bücker and G. Jung, *ChemMedChem*, 2016, **11**, 1568–1575.
99 Z. Chen, N. Ren, X. Ma, J. Nie, F.-G. Zhang and J.-A. Ma, *ACS Catal.*, 2019, **9**, 4600–4608.
100 M. I. Martinez Espinoza, L. Sori, A. Pizzi, G. Terraneo, I. Moggio, E. Arias, G. Pozzi, S. Orlandi, V. Dichiarante, P. Metrangolo, M. Cavazzini and F. Baldelli Bombelli, *Chem. – Eur. J.*, 2019, **25**, 9078–9087.
101 Z. Wang, X. Yue, Y. Wang, C. Qian, P. Huang, M. Lizak, G. Niu, F. Wang, P. Rong, D. O. Kiesewetter, Y. Ma and X. Chen, *Adv. Healthcare Mater.*, 2014, **3**, 1326–1333.
102 J. Zhang, Y. Yuan, H. Li, H. Yang, H. Zhang, S. Chen, X. Zhou, Z. Yang and Z.-X. Jiang, *J. Org. Chem.*, 2020, **85**, 6778–6787.
103 O. Munkhbat, M. Canakci, S. Zheng, W. Hu, B. Osborne, A. A. Bogdanov and S. Thayumanavan, *Biomacromolecules*, 2019, **20**, 790–800.
104 Q. Peng, Y. Li, S. Bo, Y. Yuan, Z. Yang, S. Chen, X. Zhou and Z.-X. Jiang, *Chem. Commun.*, 2018, **54**, 6000–6003.
105 L. Jamgotchian, S. Vaillant, E. Selingue, A. Doerflinger, A. Belime, M. Vandamme, G. Pinna, W. L. Ling, E. Gravel, S. Meriaux and E. Doris, *Nanoscale*, 2021, **13**, 2373–2377.
106 O. Koshkina, P. B. White, A. H. J. Staal, R. Schweins, E. Swider, I. Tirotta, P. Tinnemans, R. Fokkink, A. Veltien, N. K. van Riessen, E. R. H. van Eck, A. Heerschap, P. Metrangolo, F. Baldelli Bombelli and M. Srinivas, *J. Colloid Interface Sci.*, 2020, **565**, 278–287.
107 S. Bo, Y. Yuan, Y. Chen, Z. Yang, S. Chen, X. Zhou and Z.-X. Jiang, *Chem. Commun.*, 2018, **54**, 3875–3878.
108 Y. Zhang, S. Bo, T. Feng, X. Qin, Y. Wan, S. Jiang, C. Li, J. Lin, T. Wang, X. Zhou, Z.-X. Jiang and P. Huang, *Adv. Mater.*, 2019, **31**, 1806444.
109 H. Zhang, Q. Yu, Y. Li, Z. Yang, X. Zhou, S. Chen and Z.-X. Jiang, *Chem. Commun.*, 2020, **56**, 3617–3620.
110 H. Zhang, S. Bo, K. Zeng, J. Wang, Y. Li, Z. Yang, X. Zhou, S. Chen and Z.-X. Jiang, *J. Mater. Chem. B*, 2020, **8**, 4469.
111 K. Akazawa, F. Sugihara, T. Nakamura, H. Matsushita, H. Mukai, R. Akimoto, M. Minoshima, S. Mizukami and K. Kikuchi, *Angew. Chem., Int. Ed.*, 2018, **57**, 16742–16747.
112 S. Li, Y. Yuan, Y. Yang, C. Li, M. T. McMahon, M. Liu, S. Chen and X. Zhou, *J. Mater. Chem. B*, 2018, **6**, 4293–4300.
113 V. Dichiarante, I. Tirotta, L. Catalano, G. Terraneo, G. Raffaini, M. R. Chierotti, R. Gobetto, F. Baldelli Bombelli and P. Metrangolo, *Chem. Commun.*, 2017, **53**, 621–624.
114 O. Michelena, D. Padro, C. Carrillo-Carrión, P. del Pino, J. Blanco, B. Arnaiz, W. J. Parak and M. Carril, *Chem. Commun.*, 2017, **53**, 2447–2450.
115 J. M. Arango, D. Padro, J. Blanco, S. Lopez-Fernandez, P. Castellnou, P. Villa-Valverde, J. Ruiz-Cabello, A. Martin and M. Carril, *ACS Appl. Mater. Interfaces*, 2021, **13**, 12941–12949.
116 P. G. Argudo, M. Carril, M. T. Martín-Romero, J. J. Giner-Casares and C. Carrillo-Carrión, *Chem. – Eur. J.*, 2019, **25**, 195–199.
117 D. Xie, M. Yu, R. T. Kadakia and E. L. Que, *Acc. Chem. Res.*, 2019, **53**, 2–10.
118 Z.-X. Jiang and Y. B. Yu, *Synthesis*, 2008, 215–220.
119 Z.-X. Jiang, Y. Feng and Y. B. Yu, *Chem. Commun.*, 2011, **47**, 7233–7235.
120 E. Hequet, C. Henoumont, V. Djouana Kenfack, V. Lemau, R. Lazzaroni, S. Boutry, L. Vander Elst, R. N. Muller and S. Laurent, *Magnetochemistry*, 2020, **6**, 8.
121 M. Yu, B. S. Bouley, D. Xie and E. L. Que, *Dalton Trans.*, 2019, **48**, 9337–9341.
122 X. Yue, Z. Wang, L. Zhu, Y. Wang, C. Qian, Y. Ma, D. O. Kiesewetter, G. Niu and X. Chen, *Mol. Pharmaceutics*, 2014, **11**, 4208–4217.
123 M. Yu, D. Xie, R. T. Kadakia, W. Wang and E. L. Que, *Chem. Commun.*, 2020, **56**, 6257–6260.
124 G. Gambino, T. Gambino, R. Pohmann and G. Angelovski, *Chem. Commun.*, 2020, **56**, 3492–3495.
125 M. Yu, B. S. Bouley, D. Xie, J. S. Enriquez and E. L. Que, *J. Am. Chem. Soc.*, 2018, **140**, 10546–10552.
126 D. Xie, S. Kim, V. Kohli, A. Banerjee, M. Yu, J. S. Enriquez, J. J. Luci and E. L. Que, *Inorg. Chem.*, 2017, **56**, 6429–6437.
127 R. T. Kadakia, D. Xie, H. Guo, B. Bouley, M. Yu and E. L. Que, *Dalton Trans.*, 2020, **49**, 16419–16424.
128 D. Xie, L. E. Ohman and E. L. Que, *Magn. Reson. Mater. Phys., Biol. Med.*, 2019, **32**, 89–96.